Ultimate light-shining-through-a-wall experiments to establish QCD axions as the dominant form of dark matter

Sebastian Hoof,[1,2,*] Joerg Jaeckel,[3,†] and Giuseppe Lucente[4,3,‡]

[1]*Dipartimento di Fisica e Astronomia "Galileo Galilei," Università degli Studi di Padova, Via F. Marzolo 8, 35131 Padova, Italy*

[2]*Istituto Nazionale di Fisica Nucleare—Sezione di Padova, Via F. Marzolo 8, 35131 Padova, Italy*

[3]*Institut für Theoretische Physik, Universität Heidelberg, Philosophenweg 16, 69120 Heidelberg, Germany*

[4]*Kirchhoff-Institut für Physik, Universität Heidelberg, Im Neuenheimer Feld 227, 69120 Heidelberg, Germany*

(Received 17 July 2024; accepted 24 November 2024; published 8 January 2025)

Establishing the axion as the dark matter (DM) particle after a haloscope discovery typically requires follow-up experiments to break the degeneracy between the axion's coupling to photons and its local DM abundance. Given that a discovery would justify more significant investments, we explore the prospects of ambitious light-shining-through-a-wall (LSW) setups to probe the QCD axion band. Leveraging the excellent mass determination in haloscopes, we show how to design LSW experiments with lengths on the order of 100 km and suitably aligned magnetic fields with apertures of around 1 m to reach well-motivated axion models across up to four orders of magnitude in mass. Beyond presenting a concrete plan for postdiscovery experimental efforts, we briefly discuss complementary experiments and future directions beyond LSW experiments.

DOI: 10.1103/PhysRevD.111.015003

I. INTRODUCTION

QCD axions [1,2] and axionlike particles (ALPs) [3,4] are not only a solution to the strong *CP* problem [5,6], but also excellent dark matter (DM) candidates [7–12]. The extensive campaign of ongoing experimental searches (see, e.g., Ref. [13] for an overview) targets a broad range of axion models, e.g., Ref. [14], and importantly, realistic DM QCD axion models.

An axion discovery would be a monumental achievement and mark the first milestone in an experimental campaign focused on determining axion properties, establishing them as the dominant form of DM, and illuminating their connection to the strong *CP* problem. Incidentally, a discovery in a haloscope [15] leaves a parameter degeneracy between the axion-photon coupling $g_{a\gamma}$ and their fraction η_a of the local DM density $\rho_{\mathrm{DM},\odot}$.[1] In fact, a single experiment is rarely capable of self-consistently determining multiple axion parameters. Possible exceptions are helioscope searches [15] for axions with masses $m_a \sim 10$ meV [17,18]. However, helioscope data alone will likely yield sizable parameter uncertainties, limiting our ability to infer details of the underlying model, such as evidence for its connection to QCD.

Given these challenges, a mass determination would significantly aid the development of customized follow-up experiments and justify funding for more ambitious designs. We thus explore the potential for such follow-up experiments, starting from the information available from a haloscope discovery, which facilitate the construction of a light-shining-through-a-wall (LSW) experiment [19,20] that is guaranteed to provide a complementary probe of the newly discovered particle.[2]

The rationale behind our approach is twofold. First, the haloscope measures the product $g_{a\gamma}^2 \eta_a \rho_{\mathrm{DM},\odot}$. By using the maximum allowed value,[3] i.e., $\eta_a = 1$, we can determine a minimal value for $g_{a\gamma}$, which sets a target to guarantee a successful LSW measurement. Second, an accurate m_a measurement allows us to arrange a specific magnetic field

*Contact author: hoof@pd.infn.it

†Contact author: jjaeckel@thphys.uni-heidelberg.de

‡Contact author: lucenteg@slac.stanford.edu

[1]When encountering an axion minicluster, it may be possible to break this degeneracy with a haloscope experiment alone [16].

[2]It is presently difficult search for non-DM QCD axion models via couplings other than $g_{a\gamma}$ in laboratory-based searches, with the ARIADNE experiment Ref. [21] as a potential exception in case of an extra source of *CP* violation, e.g., Ref. [22].

[3]The probability of accidentally passing through a local overdensity, such as an axion minicluster, can be reduced by measuring for a sufficiently long time.

Published by the American Physical Society under the terms of the Creative Commons Attribution 4.0 International license. Further distribution of this work must maintain attribution to the author(s) and the published article's title, journal citation, and DOI. Funded by SCOAP³.

configuration, providing optimal sensitivity at that mass. This is important because standard LSW experiments cannot achieve the sensitivity required to reach the QCD axion band with currently available technology. Modified LSW setups can overcome this limitation, although typically only for a limited mass range, underscoring the importance of knowing m_a.

Based on this approach, we identify the QCD axion parameter space where our proposed "HyperLSW" experiments can test axions. The resulting independent measurement of $g_{a\gamma}$, in combination with the haloscope measurement, determines the local axion fraction η_a. Consequently, we can conclude whether axions are the dominant component of the local DM density or merely a smaller fraction.

Although the idea of decisively testing the QCD axion parameter space has been discussed, and initial proposals for coordinated efforts have been made, e.g., Refs. [23,24],[4] we want to push LSW experiments to the boundaries of current feasibility and explore how important questions beyond an initial discovery can be addressed.

Our strategy is outlined in Sec. II, while we summarize LSW setups and how to optimize them in Secs. III and IV, respectively. The combined HyperLSW sensitivity is discussed in Sec. V, where we also consider possible extensions and other use cases. We conclude with a summary in Sec. VI and provide additional information and supplementary computations as appendixes.

II. GENERAL STRATEGY

The cornerstone of our search strategy is a discovery in a haloscope experiment [15], which is particularly promising due to its excellent capabilities to determine m_a and the axion's direct connection to DM. To break the parameter degeneracy between $g_{a\gamma}$ and η_a, we rely on an LSW experiment [19,20], which can self-consistently determine $g_{a\gamma}$ without depending on the axion's DM nature. We identify the alternating-magnet LSW designs from Refs. [20,25] as promising, flexible options to enhance the sensitivity at specific mass values across a wide range of axion masses.

A. Haloscope discovery

Haloscope experiments can detect axions from the local DM population around Earth. We chiefly consider *resonant* searches, which are tunable and allow a superb determination of m_a, in addition to inferring $g_{a\gamma}^2\eta_a\rho_{\mathrm{DM},\odot}$. The feasibility of these searches has been demonstrated by the RBF [26] and UF [27] Collaborations and the long-running ADMX experiment [28–32]. More recently, the CAPP Collaboration [33–39] and others [40–51] have also presented competitive limits.

Haloscopes have also been recognized as tools to further study local DM properties—including the DM velocity distribution or DM substructure [16,52–54]. Indeed, the sensitivity to $g_{a\gamma}{}^2\eta_a\rho_{\mathrm{DM},\odot}$ depends on the shape of the local velocity distribution at the time of the discovery. However, once a signal is found, its time series can be analyzed to infer the local DM structure, as discussed in the works cited above. Substructure, such as streams or voids, can affect the line shape of the axion signal at high resolution, but the underlying Maxwellian shape and axion mass can still be inferred [55].

The key point for our purposes is the high precision in determining m_a after a haloscope discovery. For instance, for $m_a \sim \mu$eV and a Maxwellian halo, the expected uncertainty of m_a is well below $\Delta m_a \lesssim 1\ \mathrm{Hz} = 4 \times 10^{-15}$ eV after a year of observations (Ref. [52], Fig. 2). For intermediate m_a, this level of precision is more than sufficient for our purposes, as we explicitly demonstrate in Sec. IV and Appendix A 2. However, as discussed in Sec. V B, the upper end of masses detectable with the more advanced versions of HyperLSW would require a better mass resolution, making this case more challenging.

B. Light-shining-through-a-wall follow-up

Our follow-up experiment of choice is an LSW experiment [19,20], which both generates and detects axions via $g_{a\gamma}$. Such setups have been realized by a number of collaborations such as ALPS [56,57], OSQAR [58–60], and others [61–68] (see Ref. [69] for a review), and the currently ongoing ALPS II experiment [70] will significantly extend the LSW reach into previously untested parameter space.

Light-shining-through-a-wall experiments are typically not sensitive to QCD axion models since they would have to be extremely long when using currently available magnetic field strengths. Even then, they stop gaining in sensitivity at a length scale $\sim 2\pi\omega/m_a^2$, where ω is the angular photon frequency. This is because the axion and the photon wave increasingly go out of phase, leading to destructive interference and posing a major issue for QCD axion masses (see Sec. III).

Various modifications of the basic setup have been proposed to improve the sensitivity to larger masses and thereby in particular QCD axion models. These include optical resonators [71,72], phase shift plates [73], alternating magnet configurations [20,25], superconducting radio frequency cavities [74], magnetic field profiles [75,76], or axion magnetic resonance [77]. In this work, we utilize optical resonators, since they give an overall sensitivity improvement. In addition, we employ specific magnet configurations that allow us to resonantly enhance the sensitivity across a wide range of axion masses. The other proposals are typically more limited in their applicability,

[4]Indeed, Ref. [23] contains a suggestion for an ambitious LSW experiment ("JURA") based on FCC magnets.

although conducting a more careful analysis might prove beneficial (see Sec. VI).

Note that the downside of resonantly enhancing the signal is a rather time-consuming, difficult rearrangement of the setup when scanning across a range of axion masses. Our assumption of a haloscope discovery, and hence a precise measurement of the axion mass, eliminates this issue.

III. SUMMARY OF LSW PHYSICS

Let us summarize the basic formulas governing the axion-photon interconversion in LSW experiments—particularly for setups with multiple magnets, gaps, and possibly changing field orientations. Our discussion is largely based on Ref. [25].

Consider axions and photons propagating along the z axis inside a magnetic field of magnitude B with spatial variation $|f(z)| \leq 1$ along a perpendicular axis. For N magnets of total length $L \equiv N\ell$, the square of the axion-photon interconversion probability is given by

$$p^2_{\gamma\leftrightarrow a} = \frac{\omega^2}{\omega^2 - m_a^2}\left(\frac{g_{a\gamma}BL}{2}\right)^4 |F|^4, \tag{1}$$

with form factor

$$F \equiv \frac{1}{L}\int_0^L \mathrm{d}z\, f(z) \mathrm{e}^{\mathrm{i}qz} \tag{2}$$

and momentum transfer

$$q \equiv n_\mathrm{r}\,\omega - \sqrt{\omega^2 - m_a^2} \simeq (n_\mathrm{r} - 1)\omega + \frac{m_a^2}{2\omega}, \tag{3}$$

where n_r is the refractive index inside the magnetic fields. The approximation in Eq. (3) is valid for $m_a \ll \omega$ and matches the well-known expression for vacuum ($n_\mathrm{r} = 1$), which we assume throughout this work (see Appendix C 3 for issues related to gas-filled setups).

Allowing for gaps of size Δ between the individual magnets of length ℓ, grouped in n_g groups of alternating polarity with n_s magnets each, Ref. [25] found that the form factor can be written as

$$F_{n_\mathrm{s},n_\mathrm{g}}(x;\delta) = \frac{\mathrm{sinc}(x)}{n_\mathrm{g} n_\mathrm{s}}\frac{\tan(n_\mathrm{s} y)}{\sin(y)}\left\{\begin{array}{ll}\sin(n_\mathrm{s} n_\mathrm{g} y) & \text{if } n_\mathrm{g} \text{ is even}\\ \cos(n_\mathrm{s} n_\mathrm{g} y) & \text{if } n_\mathrm{g} \text{ is odd}\end{array}\right\}, \tag{4}$$

where we defined $\mathrm{sinc}(x) \equiv \sin(x)/x$, $x \equiv q\ell/2$, $y \equiv x(1+\delta)$, and $\delta \equiv \Delta/\ell$.

The "gapless," single-magnet limit of Eq. (4), i.e., $\delta = 0$ and $N = n_\mathrm{g} n_\mathrm{s} = 1$, reproduces the expected limits,

$$F_{n_\mathrm{s},n_\mathrm{g}}(x;\delta) \overset{\delta=0}{=} \frac{\tan(n_\mathrm{s} x)}{n_\mathrm{s} n_\mathrm{g} x}\left\{\begin{array}{ll}\sin(n_\mathrm{s} n_\mathrm{g} x) & \text{if } n_\mathrm{g} \text{ is even}\\ \cos(n_\mathrm{s} n_\mathrm{g} x) & \text{if } n_\mathrm{g} \text{ is odd}\end{array}\right\}$$
$$\overset{N=1}{=} \mathrm{sinc}(x) \equiv F_{1,1}(x). \tag{5}$$

The expected number of signal photons $\mathcal{S}$ is given by

$$\mathcal{S} \equiv \varepsilon_\mathrm{eff}\frac{P_\lambda\,\tau}{\omega}\beta_\mathrm{g}\,\beta_\mathrm{r}\,p^2_{\gamma\leftrightarrow a}, \tag{6}$$

where the effective efficiency ε_eff includes the mode overlap factor between the photon and axion modes (cf. Ref. [25]) and the detector efficiency, P_λ is the laser power, and τ is the measurement time. The quantities β_g and β_g are, respectively, the boost factors of the generation and regeneration parts of the LSW experiment, i.e., the boost factors before and after the wall. In each case, the boost factor β is given by

$$\beta^{-1} \equiv \beta_0^{-1} + \mathrm{e}^{-\zeta}, \tag{7}$$

where $\mathrm{e}^{-\zeta}$ defines the clipping losses, and β_0^{-1} summarize all other loss sources (see Appendix C 2 for details).

The clipping losses in Eq. (7) turn out to be a leading factor in limiting the reach for LSW experiments, as discussed in Sec. IV. Magnets with sufficiently large aperture could, in principle, prevent these losses and allow for the construction of LSW experiments that are hundreds of kilometers long—albeit by introducing the challenges and costs associated with large apertures. However, at such length scales another challenge becomes relevant: since LSW experiments need to follow a straight line, the curvature of Earth becomes a relevant, limiting factor. To illustrate this point, consider digging a straight tunnel of length $2L$, which emerges from Earth's surface on both ends. The depth d in the middle of the tunnel is

$$d = R_\oplus - \sqrt{R_\oplus^2 - L^2} \simeq \frac{L^2}{2R_\oplus} = 785\ \mathrm{m}\left(\frac{L}{100\ \mathrm{km}}\right)^2, \tag{8}$$

where $R_\oplus \approx 6370$ km is Earth's approximate radius. Note that d in Eq. (8) also corresponds to the maximum height of the support structures needed if HyperLSW was to be constructed on or, more accurately, tangential to Earth's surface. Therefore, and to maintain sufficient mechanical stability, a tunnel is preferable over surface construction. The deepest mine in the world, the Mponeng mine in South Africa, operates at a depth of about 4 km [78], corresponding to an experiment of total length $2L \approx 450$ km. These operations have to deal with high temperatures and other logistical challenges, but can nonetheless inform a limit on the possible length.

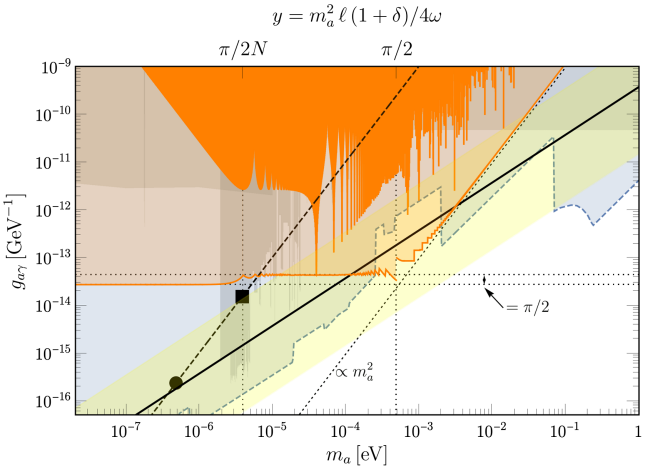

FIG. 1. Properties and scaling relations of LSW experiments. The combined addressable parameter space (light orange) for the S1 setup from Table I is compared to a single realization for $m_a = 40$ μeV (dark orange). We also show the maximal sensitivity for an LSW setup ($B = 10$ T; dashed black line) of total length of 200 km (black square) and $2R_\oplus$ (black dot), the QCD axion band (yellow region), KSVZ model (solid black line), various constraints (gray region), and projected haloscope sensitivity (light blue region, dashed line). See Fig. 3 for references.

IV. OPTIMIZING HYPERLSW SETUPS FOR QCD AXION MODELS

The main challenge for a long LSW experiment is that axion and photon waves start interfering destructively beyond a length $\sim 2\pi\omega/m_a^2$, corresponding to $x \sim \pi/2$ for a single magnet. Increasing the length beyond this point does not increase the sensitivity because the form factor decreases, thus limiting the experiment's sensitivity. This is illustrated in Fig. 1, where the dashed black line shows the 3σ median discovery sensitivity [[79], Eq. (97)] that can be reached with a single magnet of $B = 10$ T and $L \sim 2\pi\omega/m_a^2$, assuming the S1 setup in Table I for all other parameters. The black square in Fig. 1 corresponds to a total length of $2L = 200$ km, while the black dot is for $2L = 2R_\oplus$.

We can compare the LSW sensitivity to QCD axion models, which have an axion-photon coupling $g_{a\gamma}$ of

$$g_{a\gamma} = \frac{\alpha}{2\pi f_a} C_{a\gamma} = \frac{\alpha}{2\pi f_a} |E/N - C_{a\gamma,0}^{\mathrm{NLO}}|, \tag{9}$$

with anomaly ratio E/N, axion decay constant f_a, model-independent term $C_{a\gamma,0}^{\mathrm{NLO}} = (1.92 \pm 4)$ [80], and fine-structure constant $\alpha \approx 1/137$. The solid black line in Fig. 1 shows the Kim–Shifman–Vainshtein–Zakharov (KSVZ) model [81,82] ($E/N = 0$), while the yellow QCD axion band spans values $C_{a\gamma} \in [0.0722, 17.3]$. These correspond to the central 95% region from a Monte Carlo simulation of equally weighted, joint catalogs [83,84] of theoretically preferred [85,86] Dine–Fischler–Srednicki–Zhitnitsky (DFSZ) [87,88] and KSVZ axion models (available on Zenodo [89]), where we included the uncertainty of $C_{a\gamma,0}^{\mathrm{NLO}}$ via a normal distribution, $C_{a\gamma,0}^{\mathrm{NLO}} \sim \mathcal{N}(\mu, \sigma^2) = \mathcal{N}(1.92, 0.04^2)$.

From Fig. 1, it is evident that no realistic, standard LSW experiment with $B \lesssim 10$ T can probe the KSVZ benchmark model. The alternating-magnet design, however, can resonantly enhance LSW sensitivity, potentially reaching the QCD axion model band. In what follows, we detail how to achieve the optimal sensitivity for a given value of m_a in terms of the number of magnets N, grouping (given by n_s), and gap size Δ.

For instance, the opaque orange region in Fig. 1 represents the optimal sensitivity for $m_a = 40$ μeV, while the transparent orange region is the combined experimental reach of all HyperLSW experiments that could be constructed for a given m_a in that mass range. To obtain the total experimental reach, we have to distinguish three different cases, the "low," "intermediate," and "high" mass region.

We discuss these cases separately in Secs. IV A–IV C, but the main outcome can broadly be summarized as follows:

(a) The form factor in Eq. (4) is independent of m_a in the "low-mass" regime, $y \lesssim \pi/2N$, and so is the LSW experiment's sensitivity. The magnets polarizations are aligned, and gaps are minimal.

TABLE I. Benchmark setups for HyperLSW experiments, inspired by the future MADMAX and ongoing ALPS II experiments (see main text for details). The magnet designs (indicated by numbers "1" and "2") are characterized by magnetic field strength B, aperture diameter a, magnet length ℓ, and minimal gap between magnets Δ_{min}. The optics and detector depend on the laser power P_λ and wavelength λ, the intrinsic cavity boost factors in the generation (β_g) and regeneration (β_r) parts, overall efficiency $\varepsilon_{\mathrm{eff}}$, dark count rate b, and measurement time τ, for which we adopt more conservative, standard ("S") and more optimistic ("O") values. We also include the optimal/maximal HyperLSW length ($2\,z_{\mathrm{opt}}$) and the required signal strength $\mathcal{S}_{\mathrm{crit}}$ to reach our science goals.

Setup	B [T]	a [m]	ℓ [m]	Δ_{min} [m]	P_λ [W]	β_g	β_r	λ [nm]	$\varepsilon_{\mathrm{eff}}$	τ [h]	b [s^{-1}]	$2\,z_{\mathrm{opt}}$ [km]	$\mathcal{S}_{\mathrm{crit}}$
S1	9	1.3	4.0	2.0	3	10^5	10^5	1064	0.9	100	10^4	2×94	186.4
S2	11	1.8	10.0	3.0	3	10^5	10^5	1064	0.9	100	10^4	2×181	186.4
O1	9	1.3	4.0	2.0	300	10^5	10^6	1064	0.9	5000	10^6	2×79	172.5
O2	11	1.8	10.0	3.0	300	10^5	10^6	1064	0.9	5000	10^6	2×152	172.5

(b) Coherent conversion in a single magnet becomes impossible for "large" masses, $y \gtrsim \pi/2$. The optimal configuration requires fully alternating magnets and minimal gaps, leading to a sensitivity scaling of $g_{a\gamma} \sim m_a^2$ (see Sec. IV C for a derivation of the sensitivity scaling and Sec. IV D for further optimization in the transition region).

(c) In the "intermediate-mass" regime, $\pi/2N \lesssim y \lesssim \pi/2$, the optimal setups in some sense interpolate between the previous two cases, with the number of magnets per group approximately following Eq. (14). The best sensitivity in this region is approximately constant, and it is typically a factor $\pi/2 \approx 1.6$ lower than at "low" masses.

A. The low-mass region

For $m_a \to 0$, Eq. (4) goes to 0 for even n_g and to $1/n_g$ for odd n_g. The optimal setup is thus $n_g = 1$ and does not depend on the relative gap size δ. Since the conversion probability in Eq. (1) is proportional to L^2, it is optimal to chain many magnets of length ℓ with their B fields aligned in the same direction. We refer to this as the "fully aligned" setup.

The argument above ignores the clipping losses in Eq. (7), which effectively limit the total length of the LSW setup. The balance between longer setups and clipping losses results in an optimal length $z_{\rm opt}$, which generally needs to be computed numerically [25] (see Appendix C 2 for more details). An approximate value for $z_{\rm opt}$ for the production (or regeneration) part of the experiment can however be obtained following Ref. [25], Eq. (33). For instance, for $\beta_0 = 10^5$, one finds that

$$z_{\rm opt} \approx 94.2\ {\rm km}\left(\frac{1064\ {\rm nm}}{\lambda}\right)\left(\frac{a}{1.3\ {\rm m}}\right)^2, \tag{10}$$

where λ is the laser wavelength and a the aperture diameter of the magnet. Since $z_{\rm opt}$ refers to the length of only one part of the experiment, the total length of a symmetric setup would be $2 \times z_{\rm opt}$.

To determine the optimal number of magnets per part of the LSW setup, we choose

$$N = \underset{N\in\mathbb{N}}{\arg\min}|z_N - z_{\rm opt}| = {\rm round}\left(\frac{z_{\rm opt} + \Delta_{\rm min}}{\ell + \Delta_{\rm min}}\right), \tag{11}$$

where $z_N = N\ell + (N-1)\Delta$ and $\Delta_{\rm min}$ is the smallest allowed gap size. For the setup S1 from Table I, Eq. (10) gives $z_{\rm opt} \approx 94$ km, while Eq. (11) results in $N \approx 15700$.

B. The intermediate-mass region

Once $Ny \sim \pi/2$, the last factor in Eq. (4) starts oscillating, and we need to consider configurations beyond the fully aligned setup. This condition corresponds to $m_a \sim 4$ μeV for setup S1, as shown in Fig. 1.

According to Ref. [25], the maxima of Eq. (4) are close to the poles of the tangent, located at

$$x_k = \frac{(1+2k)\pi}{2n_{\rm s}(1+\delta)} \quad \text{for } k \in \mathbb{N}_0. \tag{12}$$

The largest maximum occurs for $k = 0$, where we find that (see Appendix A 1 for more details)

$$\left|\frac{F_{n_{\rm s},n_{\rm g}}(x;\delta)}{F_{1,1}(x;\delta)}\right| \to \left|\frac{1}{n_{\rm s}\,\sin(\pi/2n_{\rm s})}\right| \simeq \frac{2}{\pi} \quad (x \to x_0), \tag{13}$$

assuming that $n_{\rm s} \gg 1$ for the last approximation. Equation (13) indicates that, unless $n_{\rm s} = 1$, the sensitivity is at most a factor of $2/\pi$ lower than the optimal sensitivity in the massless limit (see Sec. IV A). This ratio is also indicated in Fig. 1.

In particular, we can achieve an optimized setup by matching $n_{\rm s}\, y = \pi/2$. This condition also connects well with the low-mass and high-mass regions since $1 \le n_{\rm s} \le N$, and it can be compactly written as

$$n_{\rm s} = \min\{N, \max\{1, {\rm round}(\pi/2y)\}\}, \tag{14}$$

leading to optimal configurations for $1/N \le 2y/\pi \le 1$, as shown by the vertical dotted lines in Fig. 1. More details on the optimization strategy for the intermediate-mass region are provided in Appendix B.

For setups other than the fully aligned one, we have to consider the width of the mass region at which we achieve optimal sensitivity. This becomes evident from Fig. 1, where the maximal sensitivity of a single configuration (solid orange region) is achieved in a rather narrow mass region. As shown in Appendix A 2, its width is

$$\frac{\Delta m_a}{m_a} \simeq \frac{\sqrt{6}}{4x_k(1+\delta)}\frac{1}{N} \approx \frac{\sqrt{6}}{2(1+2k)\pi}\frac{n_{\rm s}}{N}. \tag{15}$$

As $y_k = x_k(1+\delta) \lesssim \pi/2$ we find that, for the intermediate-mass region, we require a relative mass resolution better than

$$\frac{\Delta m_a}{m_a} \sim \frac{0.4}{N} \gtrsim 10^{-5}. \tag{16}$$

This is larger than the physical width of the axion peak in haloscope experiments and therefore problematic.

C. The high-mass region

For $y > \pi/2$, the loss of coherence is unavoidable—even for a single magnet—since the condition in Eq. (12) cannot

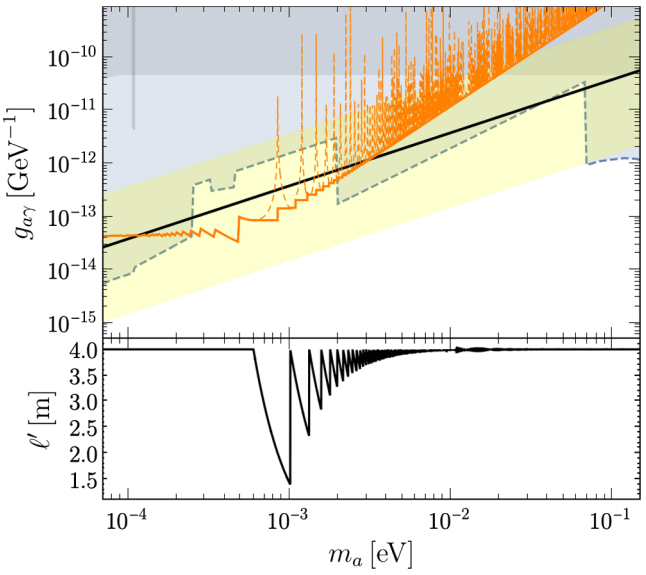

FIG. 2. Further optimization of the high-mass region. The baseline (dashed orange line) and improved sensitivity (solid orange line; top panel) for the S1 setup are shown after shortening the magnet lengths (bottom panel). We also show the QCD axion band (yellow region), KSVZ model (solid black line), various constraints (gray region), and projected haloscope sensitivity (light blue region, dashed line). See Fig. 3 for references.

be met anymore when $k = 0$. For our S1 setup, the critical mass is $m_a \sim 0.5$ meV, which is a factor of $\sqrt{N} \sim \mathcal{O}(100)$ higher than the $m_a \sim 4$ μeV threshold for the intermediate-mass region.

According to Eq. (14), when $y > \pi/2$, $n_s = 1$ and thus $n_g = N$. In this "fully alternating" setup of magnets, the poles of the tangent in Eq. (12) now correspond to maxima of the form factor in Eq. (4), as already noted in Ref. [25]. The form factor in this setup reduces to that of a single magnet of length ℓ when $x \to x_k$. Equations (1) and (6) then imply that the sensitivity can be close to N times that of a single magnet of length ℓ as long as $x \approx x_k$. We can achieve this by adjusting δ to match $x = x_k$ in Eq. (12) with the smallest possible k.

However, this approach leaves gaps in the sensitivity related to the zeros of the form factor of a single magnet of length ℓ. This is demonstrated via the dashed orange line in the upper panel of Fig. 2, which shows the sensitivity in the high-mass region the S1 setup, linked to the single-magnet form factor $F_{1,1}(x) = \mathrm{sinc}(x)$. Specifically, $\mathcal{S} \propto g_{a\gamma}^4\,\mathrm{sinc}(x)^4$, and the sensitivity worsens as $g_{a\gamma} \propto 1/\mathrm{sinc}(x) \sim m_a^2$. This explains the sensitivity gaps, related to the zeros of $F_{1,1}(x)$ at $x = k\pi$ for $k \in \mathbb{N}$. We discuss how to close these gaps in Sec. IV D.

Again, we have to consider the required mass resolution for the haloscope measurement. Equation (15) now implies a more stringent requirement because k, and x_k, are now significantly larger,

$$\frac{\Delta m_a}{m_a} \sim 10^{-6}\left(\frac{10^4}{N}\right)\left(\frac{6\text{ m}}{\ell(1+\delta)}\right)\left(\frac{\omega}{1\text{ eV}}\right)\left(\frac{2.5\text{ meV}}{m_a}\right)^2. \tag{17}$$

As a result, our "S-type" setup should not encounter serious problems up to masses of about 2.5 meV. At higher masses, however, a better resolution is required. As long as a mass resolution of $\Delta m_a/m_a \sim 10^{-9}$ to 10^{-8} can be achieved, cf. [52], Fig. 2, we may probe masses in the region $m_a \sim 25$–75 meV, which is comparable to the highest masses that can be reached with our setup (see Sec. V A). We note, however, that the mass resolution quoted above was estimated for an axion mass of 1 μeV [52], and reaching the same resolution at higher masses may be more challenging. To alleviate this issue, one may consider different detection techniques discussed in Ref. [90], or potentially obtain an even more precise mass measurement with a dedicated follow-up haloscope setup after a discovery.

D. Further optimization for high masses

As discussed in Sec. IV C, the zeros in $F_{1,1}(x)$ cannot be avoided by changing δ. One approach to address this issue, which has been successfully employed in the past, e.g., Ref. [57], involves using a buffer gas to alter the refractive index, thereby changing the momentum transfer in Eq. (3). However, due to the increased absorption and scattering losses over the long lengths of HyperLSW setups, this solution may be problematic (see Appendix C 3).

Instead, we can exploit the relation $x \propto \ell$ and adjust the length of the magnets. From Eq. (13), we know that the optimal form factor for the fully alternating configuration reduces to $F_{1,1}(x)$ at x_k. We therefore may shorten $\ell \mapsto \ell' < \ell$, such that ℓ' maximizes $F_{1,1}(x)$. To be at the maximum of the fully alternating configuration, the condition from Eq. (12) must be satisfied, implying that

$$\ell(1+\delta) = \ell'(1+\delta'). \tag{18}$$

The maxima of the form factor $|\mathrm{sinc}(x')|$ are close to

$$x'_{k'} = \frac{\pi}{2} + k'\pi \quad \text{for } k' \in \mathbb{N}, \tag{19}$$

where $x' \equiv q\ell'/2$. For each m_a, we find the largest possible value of $\ell' \le \ell$ satisfying Eq. (19), corresponding to the largest maximum of the form factor close to x_k.

While shortening of the magnet to the $k' = 1$ maximum would be optimal, doing so may be technically challenging, and we thus stay in the vicinity of the kth maximum to avoid large changes to ℓ. More details and caveats on the optimization strategy for high masses can be found in Appendix B.

The length adjustment described above and shown in the lower panel of Fig. 2 leads to the sensitivity shown in the upper panel as a solid orange line. The shortest length

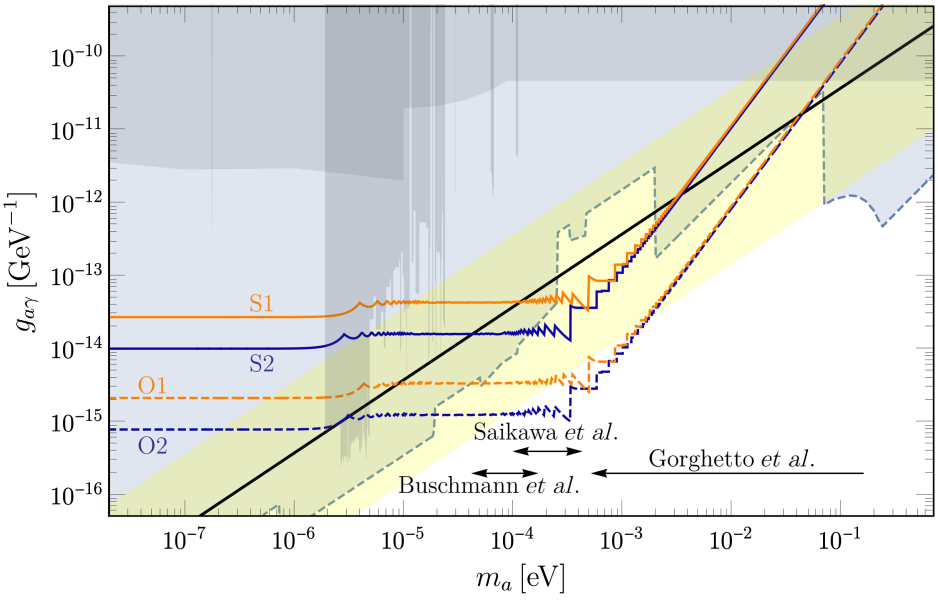

FIG. 3. Reach of HyperLSW in terms of measuring $g_{a\gamma}$ to a precision of 2% or better. Solid and dashed lines indicate the "S" and "O" setups, while orange and blue lines correspond to "type 1" and "type 2" magnets (see Table I). The QCD axion band (yellow region; defined in Sec. IV), KSVZ model (solid black line), various constraints (gray region) [26,27,29–38,40–51,93–108], and projected haloscope sensitivity (light blue region, dashed line) [40,109–118] are also shown (adapted from Ref. [119]). The black arrows indicate various predicted QCD axion mass ranges from cosmological simulations [120–124] up to the mass limit from hot dark matter overproduction [125].

required to avoid the first zero of $F_{1,1}$ is $\ell' \approx 1.5$ m—i.e., almost a factor 3 smaller than ℓ—at $m_a \approx 1$ meV, while $\ell' = \ell$ for larger m_a.

V. RESULTS AND DISCUSSION

Before constructing HyperLSW, it is crucial to ensure that we can measure η_a with sufficient precision to meet our science goals. Recall that the haloscope signal scales as $g_{a\gamma}^2 \eta_a \rho_{\mathrm{DM},\odot}$, where the average local DM density $\rho_{\mathrm{DM},\odot} = 0.3$–$0.6$ GeV/cm^3 [91,92] has sizeable systematic uncertainties.

A haloscope signal might, in principle, result from a local overdensity, such as axion miniclusters, meaning that $\eta_a > 1$. However, we can exclude this possibility by observing the signal spectrum for a longer period, beyond these usually brief and rare encounters.[5] The "worst case" scenario for HyperLSW is therefore when $g_{a\gamma}$ takes the smallest possible value for the allowed signal, corresponding to $\eta_a = 1$ and $\rho_{\mathrm{DM},\odot} = 0.6$ GeV/cm^3 (possibly multiplied with a safety factor to account for more exotic halo models). That minimal value of $g_{a\gamma}$ is the target threshold, which does not depend on the axion model.

[5]An overdensity from a "bound object" would likely also be visible as a very narrow feature in the temporal spectrum, e.g., Ref. [52].

The rationale above provides a model-independent "no-lose theorem," i.e., a clear answer to the question of whether or not it makes sense to build HyperLSW. Also note that if the target $g_{a\gamma}$ is larger than the technical sensitivity limit presented in Fig. 3, we can apply the cost-saving measures from Sec. V B 2. Assuming a QCD axion, we can also estimate $\eta_a \leq 1$ for a given cosmological scenario, which we briefly discuss in Sec. V C.

Let us now estimate the sensitivity of a HyperLSW setup. Since we assume the axion to already have been discovered, it is not meaningful to define the sensitivity in terms of a median expected limit or discovery reach. Instead, we follow the suggestion of Ref. [126], Sec. 40, and define the figure-of-merit

$$\Phi \equiv \frac{\mathcal{S}}{\sqrt{\mathcal{S}+\mathcal{B}}}, \tag{20}$$

whose inverse Φ^{-1} measures the expected relative uncertainty of the signal $\mathcal{S}$ in Eq. (6) for a background $\mathcal{B}$. Since $\mathcal{S} \propto {g_{a\gamma}}^4$, the precision for measuring $g_{a\gamma}$ is then approximately

$$\Pi \equiv \frac{\Delta g_{a\gamma}}{g_{a\gamma}} = \frac{1}{4\Phi}. \tag{21}$$

This allows us to find the critical signal threshold $\mathcal{S}$crit to achieve a desired precision Π,

$$\mathcal{S}_{\rm crit} = \frac{1}{32\Pi^2}(1+\sqrt{1+64\,\mathcal{B}\,\Pi^2}). \tag{22}$$

The choice of Π depends on our science goals. We can assume that the haloscope provides a precise estimate for $g_{a\gamma}^2\eta_a\rho_{\rm DM,\odot}$ due to the high statistical significance required for a detection, and HyperLSW can also potentially estimate $g_{a\gamma}^4$ very precisely. The uncertainty on η_a will thus mainly arise from the systematic spread in $\rho_{\rm DM,\odot}$ estimates, which roughly lie within a factor of 1.3 within the intermediate value of $\rho_{\rm DM,\odot} = 0.45\ {\rm GeV/cm^3}$. Potential future reductions in the systematic uncertainties of $\rho_{\rm DM,\odot}$ justify aiming for a precision of around 20% for η_a ($\Pi = 10\%$), aligning the statistical uncertainty of η_a with the systematic uncertainty of $\rho_{\rm DM,\odot}$.

While going beyond that level is not indicated as far as η_a is concerned, an alternative science target could be to measure $g_{a\gamma}$ at the level of theoretical uncertainty for the QCD axion. This may allow us to infer the corresponding E/N, narrowing down the underlying axion model from the available model catalogs [83,84]. The limiting factor is the theoretical uncertainty from axion-meson mixing, encoded in the uncertainty on $C_{a\gamma,0}^{\rm NLO}$ in Eq. (9). For instance, for the KSVZ model ($E/N = 0$), we would require a target precision of $\Pi = 2\%$.

Given the effort required to build HyperLSW, we use $\Pi = 2\%$ as a more ambitious target.

A. Sensitivity for benchmark setups

In addition to the S1 setup, already introduced in previous sections, we provide further benchmark setups in Table I. In particular, the letters "S" and "O," respectively, denote configurations with more conservative ("standard") and more optimistic experimental parameters, while the numbers 1 and 2 indicate different magnet designs. The values for "type 1" and "type 2" magnets are inspired by prototype magnets for the MADMAX experiment [127,128]. We also impose a minimal gap size that is somewhat larger than a to ensure a good magnetic field quality within the gaps (see, e.g., Ref. [129]). Setups with "type 2" magnets assume both a larger aperture diameter a and length ℓ. They thus lead to longer experimental setups (cf. $z_{\rm opt}$ column in Table I) and better sensitivity in the low-mass and intermediate-mass regions compared to "type-1" magnets. However, due to their larger ℓ, "type-2" magnets do not improve the sensitivity in the high-mass regime since the condition $y > \pi/2$ is already fulfilled at smaller masses.

The nonmagnet parameters that we consider are largely inspired by the achieved or projected capabilities of the ALPS II experiment (Ref. [70], e.g., Table 1).

In Fig. 3, we show the sensitivity for all benchmark setups. They can achieve QCD axion sensitivity (with respect to our target precision) over a significant mass range and, in particular, KSVZ axions sensitivity in the following mass ranges:

$$m_a^{\rm KSVZ} \in [0.11, 3.4]\ {\rm meV} \quad \text{for setup S1},$$
$$m_a^{\rm KSVZ} \in [0.002, 45]\ {\rm meV} \quad \text{for setup O2}.$$

As in previous figures, we indicate the region that can be probed by existing (gray regions) and proposed (light blue region delimited by a dashed line) haloscope experiments. The overlapping regions of the projected sensitivity for future haloscopes and our benchmark setups are the currently most intriguing ones for envisioning HyperLSW due to a possible future a discovery and hence the required precise mass measurement. The KSVZ mass ranges above can further be compared to future bounds from cosmology, which could limit $m_a \lesssim 40$ meV [130]. Regarding these mass values, we highlight the existence of the "meV gap" in haloscope searches for large parts of the QCD axion band. Closing this gap is technologically challenging but would be required to realize the full potential for HyperLSW.

B. Potential issues and extensions

Having demonstrated the general feasibility of HyperLSW under idealized conditions, we now discuss some of the potential issues for a realistic implementation.

1. Experimental uncertainties

Reaching the QCD axion band relies on resonantly enhancing the LSW setup by specific magnet arrangements, in particular at larger m_a. We thus have to ensure the following:

(a) The width of the resonance peaks is larger than the precision of the haloscope measurement.
(b) The unavoidable errors from magnet imperfections and positioning do not spoil the resonance.

In Appendix A 2, we estimate the width of the resonance peaks and find that, thanks to the superb mass resolution of haloscopes, sub-meV masses are generally unproblematic. For larger masses, we require $\Delta m_a/m_a \sim 10^{-9}$ to 10^{-8}, as discussed in Sec. IV C.

In Appendix D, we compute analytical estimates and perform Monte Carlo simulations to estimate the systematic shift and uncertainty on the form factor $|F|$ due to various sources of uncertainties. We find that random errors in the absolute magnet positioning of order $\mathcal{O}(1\ {\rm cm})$ become problematic for $m_a \gtrsim 4$ meV. At larger masses, we would need to reduce the positioning errors. For instance, to reach $m_a = 40$ meV, Eq. (D3) requires positioning errors of order 100 μm.

Regarding misalignment and size differences in the magnetic field profiles, issues arise for $m_a \gtrsim 0.5$ meV. Apart from also reducing the uncertainties, we can measure and thus characterize the magnetic field profiles of all

magnets and subsequently compensate any undesired phase shifts to achieve the target sensitivity. While this increases the setup's complexity, we deem such efforts to be realistically achievable.

2. Cost and construction time estimates

Achieving the highest possible sensitivity in HyperLSW experiments incurs significant construction costs, primarily driven by tunneling and magnet construction.

The cost of a single magnet is roughly proportional to the stored magnetic energy in the magnet volume, which scales as $B^2\ell a^2$. Since the setups in Table I are inspired by the magnet designs for the future MADMAX experiment, we can use the related design studies to estimate the costs. Given the anticipated unit cost of about 0.01 GEUR (1 GEUR = one billion euro) [127,128], the total cost for N magnets scales as

$$C_{\rm magn} \sim 10\ \text{GEUR}\left(\frac{B}{9\ \text{T}}\right)^2\left(\frac{\ell a^2}{6.8\ \text{m}^3}\right)\left(\frac{N}{1000}\right). \tag{23}$$

Tunneling cost can, in principle, be compared by normalizing to the excavated volume. However, it does not necessarily scale linearly with the cross sectional area [[131] chart G.1] or length [[131] chart G.2]. The former is relevant for HyperLSW due to the large aperture of the magnets, while the latter is due to planning costs and other expenses, which disproportionally affect shorter tunnels of length $z \lesssim 25$ km [[132] chart 7.5]. Since we anticipate much longer setups, we may assume a linear scaling with the total length of the experiment. As a reference, the cost for a future "Hyperloop" long-distance transport tunnel with a 6.5 m diameter has been estimated to cost around 8.4 GEUR/100 km [132,133].[6] This is in line with the cost of the Gotthard Base Tunnel (7.6 GEUR/100 km; total length of all tunnels: 152 km; total cost of 9.5 GCHF at 1998 price levels) [134] or estimated cost of the Brenner Base Tunnel (4.6 GEUR/100 km; total length of all tunnels: 230 km; total cost of 10.5 GEUR at 2023 levels).[7] Thus, for an experiment of total length Z, we estimate the tunneling cost to be

$$C_{\rm tunnel} \sim 10\ \text{GEUR}\left(\frac{Z}{100\ \text{km}}\right). \tag{24}$$

Ignoring the costs of the optical components and operations, the two benchmark setups would cost

$$S_1\colon\ 200\ \text{GEUR}, \qquad S_2\colon\ 1000\ \text{GEUR}.$$

These are, of course, rather crude estimates, and more refined estimates will depend on the experiment's location and other factors.

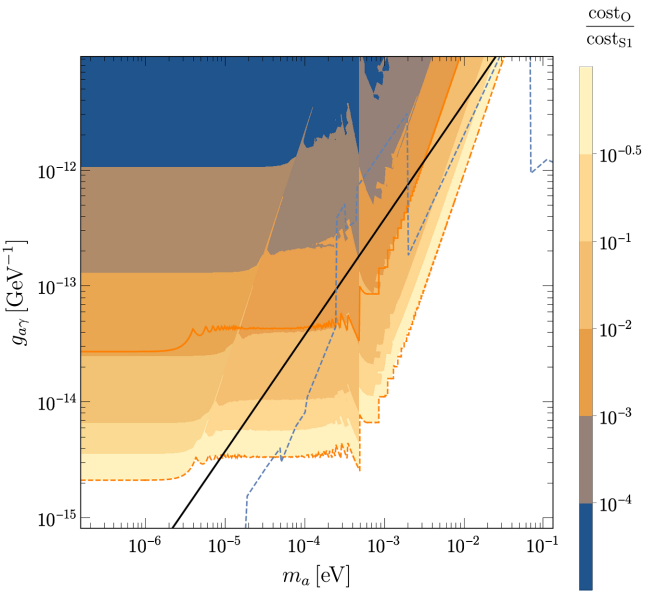

FIG. 4. Contour plot of the O-type HyperLSW cost and $a < 1.3$ m relative to the cost of the corresponding S1 setup. The KSVZ model (solid black line) and and projected haloscope sensitivity (dashed light blue line) are also shown (see Fig. 3 for references).

3. Potential cost reductions

The tentatively high costs of HyperLSW may be justified by additional uses for the facility, which we briefly discuss in Sec. V C. However, there is also potential for cost savings due to mass production of the magnets, which we did not take into account in our estimates.

Moreover, if the haloscope measurement suggests a relatively high $g_{a\gamma}$ target, we could scale down HyperLSW while still achieving its primary physics goals. Specifically, one could reduce the number of magnets or use a smaller aperture a to save money since, according to Eq. (10), the sensitivity scales as $g_{a\gamma} \propto (N\ell)^{-1} \sim a^{-2}$ if $N\ell \sim z_{\rm opt}$. If the magnet cost dominates, $C_{\rm magn} > C_{\rm tunnel}$, and the total cost approximately scales as B^2a^4, implying $g_{a\gamma} \propto C_{\rm magn}^{-1/2}$. For $C_{\rm tunnel} > C_{\rm magn}$, costs will scale as $C_{\rm tunnel} \propto z \sim a^2$, implying $g_{a\gamma} \propto C_{\rm tunnel}^{-1}$.

Note that the choice of setup plays a crucial role in reducing costs by allowing shorter experiments. Consider the contour plot in Fig. 4, which shows the cost of O-type optical setups and $a < 1.3$ m relative to the cost for the S1 setup at each value of m_a. The solid orange line represents the S1 sensitivity, while the dashed orange line corresponds to the O1 sensitivity. It is evident that the O-type optical

[6]Unless stated otherwise, all costs are adjusted to January 2024 price levels.

[7]See the project website at https://www.bbt-se.com/en/tunnel/project-overview/ for information and updates on the Brenner Base Tunnel.

setup offers an order of magnitude better sensitivity than the S1 setup without a significant increase in cost, while the S1 sensitivity could be reached at around 100 times lower costs, confirming the expected "magnet-driven" scaling. For $g_{a\gamma} \gtrsim 10^{-14}$ GeV^{-1}, we enter the regime of "tunnel-driven" costs.

Further cost reduction is possible by using a laser with a shorter wavelength. Equation (10) tells us that $z \propto \lambda^{-1} a^2$, suggesting that halving λ would permit smaller aperture a by a factor of $\sqrt{2}$ while maintaining the same experimental length and thus yielding the same sensitivity at half the cost.[8] The mass reach would also slightly increase due to the reduced $q \sim m_a^2/2\omega$.

Apart from costs, other factors to consider are the time and resources required to produce potentially tens of thousands of magnets. Past experience at the LHC has shown that, after a fairly predictable "learning curve" [135], three suppliers combined could produce around 400 magnets per year [136]. The proposed FCC-hh experiments estimate a series production time of about six years for around 4700 magnets, noting that the choice of superconducting material must be considered carefully due to supply chain issues [137]. The timescales for magnet production are of the same order of magnitude as those required for the tunnel construction. For instance, constructing the Gotthard Base Tunnel (total length of tunnels: 152 km) took almost 17 years [134], while construction of the Brenner Base Tunnel (total length of tunnels: 230 km) is expected to take 25 years (see footnote 7).

C. Other use cases for the HyperLSW facility

While it is premature to build a detailed physics case for HyperLSW, we nonetheless want to provide additional motivation for the significant investment required for such a facility.

1. Uses related and complementary to axion physics

A haloscope discovery of QCD axions would not only reveal m_a but also the energy scale related to the Peccei–Quinn (PQ) mechanism, set by the axion decay constant f_a, thanks to the relation [80,138]

$$m_a = (5.69 \pm 5)\ \mu\text{eV}\left(\frac{10^{12}\ \text{GeV}}{f_a}\right). \tag{25}$$

This connection by itself could already tell us a lot about axion cosmology (see, e.g., Refs. [139,140] for reviews), as the extremely precise m_a measurement would constrain f_a at the level of 0.9%. We can consider two primary cosmological scenarios for QCD axions, one where the PQ symmetry breaks before the end of inflation and remains unbroken thereafter and another where it breaks after inflation.[9]

In the preinflationary scenario, the initial field value is a random variable, uniformly distributed in the canonical range of $\theta_{\text{ini}} \sim \mathcal{U}(-\pi, \pi)$ [11]. There is also a contribution from isocurvature fluctuations in this scenario which, depending on the detected value of m_a, could imply fine-tuning that is worse than the strong CP problem itself, e.g., Ref. [142]. In the postinflationary scenario, we consider an ensemble average of random initial field values, which is equivalent to single, fixed value of $\sqrt{\langle\theta_{\text{ini}}^2\rangle} \approx 2.6$ [11], with additional contributions from topological defects. Recent simulations of axion production from cosmic string decays are not in full agreement between each other, but suggest that these contribution will increase η_a [120–124,143–147]. A precise measurement of m_a could favor one of the two cosmological scenarios and potentially allow us to estimate η_a rather than use the limiting case of $\eta_a = 1$ in Sec. V to justify construction of HyperLSW.

Furthermore, since $g_{a\gamma} \propto 1/f_a$, HyperLSW provides insights into the nature of the newly discovered particle—although it cannot prove that the new particle is a QCD axion. Using Eq. (9), we can estimate E/N and, using the QCD axion model catalogs [83,84], we can potentially identify only a few candidate UV models, potentially increasing our confidence in the axion's QCD nature. A similar approach was proposed in Ref. [148] for helioscope searches, which look for axions produced in the Sun. Previous campaigns by the Brookhaven [149], Sumico [150–152], and CAST [153–158] Collaborations will be extended by the upcoming IAXO experiment [159–161], which may measure the axion's couplings [17] or mass [18]. An LSW measurement of $g_{a\gamma}$ and, if m_a is in the suitable mass range, a haloscope measurement of m_a may further enhance IAXO's capabilities to fit g_{ae}, which also depends on f_a via $g_{ae} \propto 1/f_a$. Furthermore, if IAXO data prefer a dominant axion-photon coupling, we may establish evidence for KSVZ models. However, such detailed studies are beyond the scope of this work.

2. Use cases beyond axions

The specific magnet configuration required to reach HyperLSW's primary physics goals can be rearranged to achieve other objectives—similar to more generic LSW experiments. For instance, photons and gravitons can interconvert inside a magnetic field via the (inverse) Gertsenshtein effect [162], making it possible for LSW experiments to detect gravitational waves (GWs) [163]. The minimal detectable GW amplitude scales as $(BL)^{-1}a^{-1/2}$, making HyperLSW, in principle, very sensitive to GWs

[8] This is also suggested in Ref. [23], but to permit an increase in the length.

[9] An intermediate scenario [141] or various other modifications are also possible (see Ref. [24], Sec. 41, for a review).

emitted below the limit set by big bang nucleosynthesis (cf. Ref. [163], Fig 5)—albeit only with extremely narrow spectral range if all magnets are used.

The magnets used in HyperLSW could also be repurposed for other (axion) experiments. Examples are CAST used prototype magnets from the LHC [153], and the ongoing ALPS II experiment used modified magnets from the decommissioned HERA accelerator [164].

The larger aperture diameter of our magnets might enable previously impossible use cases, such as magnetic resonance imaging—although the required magnetic field homogeneity would pose significant challenges.

The infrastructure of HyperLSW could also host other particle physics experiments. Examples include the proposed International Linear Collider [165–167] or the Einstein Telescope [168–170], both of which may use parts of the HyperLSW tunnel. Similarly, "Hyperloop" long-distance transport systems could potentially fit inside the tunnel, even if entirely straight tunnels are not necessarily preferred due to geological or financial considerations [171]. The location of HyperLSW could be chosen by bearing such potential future uses in mind.

VI. CONCLUSIONS

Assuming the discovery of (QCD) axions in a haloscope, we have presented a blueprint for constructing HyperLSW, an ambitious light-shining-through-a-wall (LSW) experiment aimed at probing axion properties with a purely laboratory-based setting. Haloscopes directly measure the axion mass m_a as well as the product $g_{a\gamma}^2\eta_a\rho_{\mathrm{DM},\odot}$ of the axion-photon coupling $g_{a\gamma}$, the axion dark matter (DM) fraction η_a, and the local DM density $\rho_{\mathrm{DM},\odot}$. Knowledge of m_a then allows for the construction of a HyperLSW follow-up experiment, which would directly measure $g_{a\gamma}$. Together, these measurements determine the axion DM density $\eta_a\rho_{\mathrm{DM},\odot}$. The key findings and implications of our study are summarized as follows:

(a) Haloscopes only measure m_a and signals $\propto g_{a\gamma}^2\eta_a$, necessitating an independent measurement of $g_{a\gamma}$ to establish axions as the dominant form of DM.
(b) Magnets with large aperture diameter $\gtrsim$1 m enable LSW experiments with total lengths $\gtrsim$100 km.
(c) HyperLSW can probe QCD axions by optimizing the magnetic field configuration for a known m_a. Its most ambitious incarnations achieve KSVZ sensitivity for 2 μeV $\lesssim m_a \lesssim$ 45 meV.
(d) The resonant nature of HyperLSW at large $m_a \gtrsim \mathcal{O}(\mathrm{meV})$ requires a nontrivial haloscope mass resolution, as well as high levels of precision in the magnet manufacturing, arrangement, and quality control, which are realistically achievable through error control or precise magnetic field profiling.
(e) HyperLSW setups are ambitious and costly but do not require any technological breakthroughs; any technological advancements would however further extend their reach or reduce costs.

HyperLSW shares similarities with other large-scale physics experiments, such as the LHC—also with regard to a "no-lose theorem." While HyperLSW may not match the versatility of other experimental facilities, its potential extensions and alternative uses mentioned in Sec. V C should be explored more extensively. In fact, while the LSW designs investigated here offer favorable sensitivity, across a wide mass range, we did not explore all alternatives—LSW or otherwise—which could potentially be cheaper or more effective to study axions, in particular, for larger m_a and $g_{a\gamma}$. One interesting option could be a helioscope such as IAXO [159,160], especially in the range $m_a \gtrsim 10$ meV where the realization of HyperLSW setups is more difficult. IAXO could also benefit from knowing m_a since the coupling measurement may become more precise compared to an *a priori* unknown value of m_a [17,18].

To conclude, this study represents one of the first concrete explorations of necessary follow-up strategies in case of an axion discovery, which, to our knowledge, has not yet been investigated in detail in the literature.

ACKNOWLEDGMENTS

We are very grateful to Gianfranco Bertone for encouraging us to be ambitious and to push to the boundaries of experimental feasibility, thus initiating this project. For helpful discussions, we would like to warmly thank Gianluigi Arduini, Laura Covi, Loredana Gastaldo, Erik W. Lentz, Axel Lindner, Edoardo Vitagliano, and the staff at the Multiphysics Division of Bilfinger Nuclear & Energy Transition GmbH. S. H. has received funding from the European Union's Horizon Europe research and innovation programme under the Marie Skłodowska-Curie Grant Agreement No. 101065579. G. L. is grateful to Bilfinger Nuclear & Energy Transition GmbH for hospitality during the last stages of this work. G. L. and J. J. are supported by the European Union's Horizon 2020 Europe research and innovation programme under the Marie Skłodowska-Curie Grant Agreement No. 860881-HIDDeN. This article is based upon work from COST Action COSMIC WISPers CA21106, supported by COST (European Cooperation in Science and Technology).

APPENDIX A: FURTHER DETAILS ON THE FORM FACTOR F

In this appendix, we take a closer look at the maxima of the form factor $|F|$ in Eq. (4), which can be approximately identified with the poles of $\tan(\cdot)$ [25]. This is helpful as numerical evaluation of F is challenging due to the poles and zeros of the trigonometric functions. We therefore have to examine the region around the maxima, particularly to

estimate their width compared to the precision available from haloscopes.

1. Limits and (approximate) maxima

Consider the fully aligned setup ($n_g = 1$), where

$$F_{N,1}(x) = \frac{\mathrm{sinc}(x)}{N}\frac{\sin(Ny)}{\sin(y)}, \tag{A1}$$

and where $y \equiv x(1+\delta)$. The maxima of Eq. (A1) correspond to the zeros of $\sin(y)$,

$$x_k = \frac{k\pi}{1+\delta} \quad \text{for } k \in \mathbb{N}_0. \tag{A2}$$

At these maxima, the form factor reduces to that of a single magnet, $F_{N,1}(x_k) = F_{1,1}(x_k) = \mathrm{sinc}(x_k)$. The absolute maximum occurs at $x_0 = 0$, implying that this setup leads to the best sensitivity in the low-mass limit $Ny \ll 1$, i.e., $m_a \ll 2\sqrt{\omega/N\ell(1+\delta)}$, where $|F| = 1$.

For $n_g > 1$, the maxima of Eq. (4) are close to the poles of the tangent, located at

$$x_k = \frac{(2k+1)\pi}{2n_s(1+\delta)} \quad \text{for } k \in \mathbb{N}_0. \tag{A3}$$

Choosing $k = 0$ again leads to the largest form factor. Substituting $x = q\ell/2$ with $q \approx m_a^2/4\omega$, the maximum is found at

$$m_a = \sqrt{\frac{2\pi\omega}{n_s\ell(1+\delta)}}, \tag{A4}$$

or, equivalently, for the gap parameter

$$\delta = \frac{2\pi\omega}{n_s\ell m_a^2} - 1. \tag{A5}$$

In the limit $x \to x_0$, the form factor converges to

$$|F| \to \frac{1}{n_s}\left|\mathrm{sinc}\left(\frac{\pi}{2n_s(1+\delta)}\right)\frac{1}{\sin\left(\frac{\pi}{2n_s}\right)}\right|, \tag{A6}$$

matching the expression in Ref. [25], Eq. (24), after inserting the definition of q.

The maximum of $|F|$ approaches x_0 as n_g increases, as illustrated in Fig. 5 for $n_s = 10$, $\delta = 1$, and various values of n_g. The largest discrepancy between $|F(x_0)|$ (gray lines) and the true maximum is found for $n_g = 2$ (red lines). As n_g increases, the discrepancy diminishes. For the example in Fig. 5, we confirmed numerically that the discrepancy is less than 2% for the location of the maximum and less than 1% for the value of the form factor when $n_g > 8$. The shift

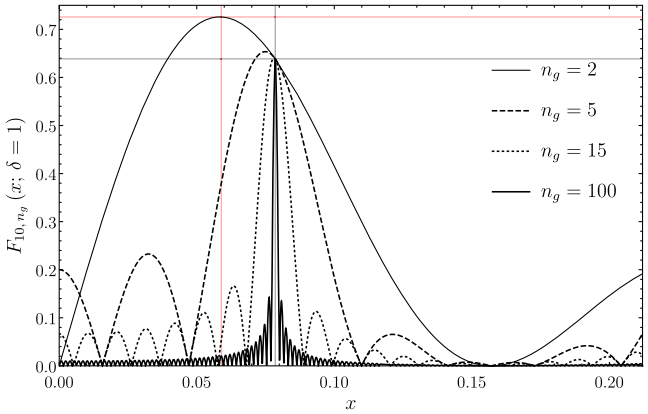

FIG. 5. Form factor $|F|$ for $n_s = 10$, $\delta = 1$, and various n_g values. The black lines correspond to the $k = 0$ pole of the tangent, cf. Eqs. (A3) and (A6), while the red lines are defined by Eqs. (A7) and (A8).

with respect to the true location of the maximum and its value is almost independent of n_s and δ and decreases slightly for larger values.

For $n_g = 2$, where the discrepancy between x_0 and the true maximum is largest, we can refine our estimate by observing that, for $n_s > 1$, the location and value of the absolute $|F|$ maximum are well approximated by

$$\tilde{x}_0 = \frac{3}{4}\frac{\pi}{2n_s(1+\delta)}, \tag{A7}$$

$$|F_{2,n_s}(\tilde{x}_0)| = \frac{2(2+\sqrt{2})}{3\pi}\left|\frac{(1+\delta)\sin\left(\frac{3\pi}{8n_s(1+\delta)}\right)}{\sin\left(3\pi/8y\right)}\right|. \tag{A8}$$

The red lines in Fig. 5 correspond to Eqs. (A7) and (A8), improving the estimate for the maximum from Eqs. (A3) and (A6) (gray lines).

The condition in Eq. (A4) implies that the largest accessible mass is $m_a = \sqrt{2\pi\omega/[\ell(1+\delta_{\min})]}$, where $\delta_{\min}$ is the minimum gap size. To probe larger masses, the fully alternating setup ($n_s = 1$) has to be used, with gap sizes matching the local maxima of $|F|$, located at x_k in Eq. (A3). With q given by Eq. (3),[10] the corresponding gap sizes are

$$\delta_k = \frac{(2k+1)\pi}{q\ell} - 1. \tag{A9}$$

The local maxima for $|F|$ converge to

$$|F_{1,N}(x;\delta_k)| \to |\mathrm{sinc}(x_k)| \quad (x \to x_k), \tag{A10}$$

[10]When requiring high accuracy, the approximation $q \approx m_a^2/2\omega$ should be avoided for $m_a \gtrsim 10$ meV.

showing that, in the fully alternating configuration of N magnets with gap size δ_k, the maxima of the form factor correspond to the value of the form factor of a single magnet of length ℓ.

2. Expansion around the poles x_k

To assess if the haloscope mass determination is precise enough to realize HyperLSW, we need to estimate the width of the form factor peaks around the poles x_k. This is especially crucial for fully alternating setups that probe large masses due their resonant nature. A second-order expansion in $\xi_k \equiv x - x_k$ is sufficient for narrow peaks,

$$\left|\frac{F_{1,N}(x)}{F_{1,N}(x_k)}\right| = 1 + a^{(1)}_{N,1}\xi_k + a^{(2)}_{N,1}\xi_k^2 + \mathcal{O}(\xi_k^3), \tag{A11}$$

$$a^{(1)}_{N,1} = \cot(x_k) - \frac{1}{x_k}, \tag{A12}$$

$$a^{(2)}_{N,1} = -\frac{1}{3}(N^2-1)(1+\delta)^2 - 1 - \frac{2a^{(1)}_{N,1}}{x_k}, \tag{A13}$$

with $\cot(x) \equiv 1/\tan(x)$ and where, unlike in Eq. (4), the result is same for even and odd $n_g = N$.[11]

Solving for the full width at half maximum, defined via $|F(x)/F(x_k)| = 1/2$, gives solutions $x_\pm$. The haloscope's mass sensitivity can then be compared to the *half width* at half maximum,

$$\frac{\Delta m_a}{m_a} \approx \frac{\Delta q}{2q} = \frac{\Delta x}{2x} \approx \frac{x_+ - x_-}{4x_k}. \tag{A14}$$

We find that

$$\frac{x_+ - x_-}{4x_k} = \frac{\sqrt{3}}{4}\frac{\sqrt{[2(N^2-1)(\delta+1)^2 + 3(2+\cot^2(x_k))]x_k^2 + 6\cot(x_k)x_k - 9}}{[(N^2-1)(\delta+1)^2+3]x_k^2 + 6\cot(x_k)x_k - 6} \simeq \frac{\sqrt{6}}{4x_k(1+\delta)}\frac{1}{N} \quad (N\to\infty). \tag{A15}$$

The width of in Eq. (A15) thus decreases as N increases. As further discussed in Secs. IV B and IV C, this may imply fairly stringent requirements on the mass resolution of the preceding haloscope measurement. In particular, at higher masses $\gtrsim$few meV, this may be a nontrivial prerequisite for building HyperLSW.

APPENDIX B: OPTIMIZATION ALGORITHM FOR HYPERLSW

The optimal parameter values for $\boldsymbol{\theta} = (n_g, n_s, \delta)$, denoted by $\boldsymbol{\theta}_{\rm opt} = (n_{g,\rm opt}, n_{s,\rm opt}, \delta_{\rm opt})$, can be found by numerically maximizing the expected signal $\mathcal{S} \propto g_{a\gamma}^4$ for a given value of m_a. Such mixed-integer optimization problems are typically challenging. Fortunately, as shown in Appendix A, the poles x_k are very close to the true location of the maxima of $|F|$, especially for large $N = n_g \times n_s$. Here, we detail how to exploit this via an algorithmic approach, with results for the S1 setup (see Table I) shown in Fig. 6.

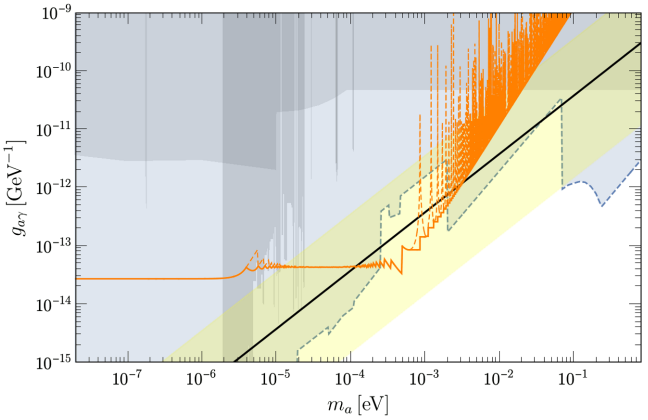

FIG. 6. Sensitivity for the S1 setup. The dashed line corresponds to the sensitivity for the $\boldsymbol{\theta}_{\rm opt}$ parameters described in Appendix B. The QCD axion band (yellow region), KSVZ model (solid black line), various constraints (gray region), and projected haloscope sensitivity (light blue region, dashed line) are also shown (see Fig. 3 for references).

1. Intermediate-mass region

The values for $\boldsymbol{\theta}_{\rm opt}$ are determined by choosing the longest total length while avoiding clipping losses, i.e., $N\ell \sim z_{\rm opt}$. In the "intermediate-mass region" ($\pi/2N < y < \pi/2$), we find the smallest value of the optimal $\delta_{\rm opt} \geq \delta_{\rm min}$ for a fixed value of m_a from Eq. (A5) by varying n_s. This gives us values for $(\delta_{\rm opt}, n_{s,\rm opt})$. We then compute $n_{g,\rm opt}$ as $n_{g,\rm opt} = \lfloor z_{\rm opt}/n_{s,\rm opt}\ell(1+\delta_{\rm opt})\rfloor$, where $\lfloor\cdot\rfloor$ indicates the floor function. In other words, we find the largest number of groups n_g with n_s magnets per group fitting in $z_{\rm opt}$. The resulting setup is shown as dashed orange lines in the intermediate-mass region in Fig. 6. For masses with the same $n_{s,\rm opt}$, the best sensitivity is achieved for $\delta_{\rm opt} \to \delta_{\rm min}$ since this leads to larger $n_{g,\rm opt}$. This explains the spikes observable at the end of the intermediate-mass region, $y \sim 1$, which are unavoidable due to fine-tuning effects: the form factor is highly

[11]Evaluating the second derivatives requires multiple applications of L'Hôpital's rule.

oscillatory and spiky, and small changes in n_g, n_s, and δ thus lead to a huge loss in sensitivity.

2. Further improvements

The above procedure is not entirely effective at the beginning of the intermediate-mass region, where $n_{g,opt} \sim 1$. Indeed, in this case, the difference $z_{opt} - n_{g,opt} n_{s,opt} \ell (1+\delta) \lesssim n_{s,opt} \ell (1+\delta_{opt})$ is sizable, leading to an inefficient configuration much shorter than z_{opt} (cf. dashed orange line in the region of $m_a \approx 5$–10 μeV).

To improve the setup, we follow an alternative procedure. As shown in Fig. 5, for low values of n_g, the full width at half maximum is larger than the one found higher values of n_g. Therefore, one can find a configuration $\boldsymbol{\theta}'_{opt} = (n'_{g,opt}, n'_{s,opt}, \delta'_{opt})$ for which the form factor $|F|$ is maximized at $x'_a \neq x_a \approx m_a^2 \ell / 4\omega$, but with better sensitivity at m_a compared to the $\boldsymbol{\theta}_{opt}$ configuration. Since we want to achieve a total length close to z_{opt} by adding more magnets, we fix $n'_{g,opt} = n_{g,opt} + 1$ and $n'_{s,opt} = \lfloor z_{opt} / n'_{g,opt} \ell (1+\delta_{min}) \rfloor$. We then compute $\delta'_{opt} = z_{opt} / (n'_{g,opt} n'_{s,opt} \ell) - 1$. Finally, for each m_a, the HyperLSW sensitivity is defined as the lowest value of $g_{a\gamma}$ which can be probed with $\boldsymbol{\theta}_{opt}$ and $\boldsymbol{\theta}'_{opt}$ configurations. We show the outcome of this procedure as a solid line in the intermediate-mass region of Fig. 6. These differ from the $\boldsymbol{\theta}_{opt}$ parameters (dashed lines) only at the beginning of the intermediate-mass region, implying that $\boldsymbol{\theta}'_{opt}$ leads to a better sensitivity for small n_g, while $\boldsymbol{\theta}_{opt}$ is better at larger n_g.

3. High-mass region

For higher masses, $y > \pi/2$, we slightly modify the intermediate-mass-region procedure for $\boldsymbol{\theta}_{opt}$ by finding the lowest value of k for which $\delta_k \geq \delta_{min}$ in Eq. (A9). For this value of δ_k, the form factor reduces to the single-magnet form factor $F_{1,1}$ as shown in Eq. (A10), and the sensitivity is given by the dashed orange line in Fig. 6 at masses $m_a \gtrsim 1$ meV. To avoid the zeros of $F_{1,1}$, we propose to shorten the length of the single magnet, $\ell \mapsto \ell'$ (see Sec. IV D). The resulting sensitivity is shown as a solid orange line in Fig. 6. In this case, ℓ' is chosen to maximize $|F_{1,1}|$, whose maxima are given by Eq. (19), while fulfilling the condition in Eq. (12).

A word of caution for masses corresponding to $x \lesssim 4.49$, which is the location of the second local maximum of $|\mathrm{sinc}(x)|$ (the first maximum is at $x = 0$). For these masses, the previous maximum would correspond to $\ell' = 0$, and we need to employ a different strategy. The high-mass regime starts at $m_{a,crit} = \sqrt{2\pi\omega/\ell(1+\delta_{min})}$, while the best sensitivity is reached at $m_a^* = \sqrt{2\pi\omega/\ell}$, due to the product $L^4 |F_{1,1}|^4$ in the computation of $p^2_{\gamma\leftrightarrow a}$ in Eq. (1). Therefore, for $x \lesssim 4.49$, for masses $m_{a,crit} < m_a < m_a^*$ shortening the magnet length would not give any improvement, while for larger masses one can improve the sensitivity by choosing a length $\ell' = q(m_a^*)\ell / q(m_a)$. This leads to the sensitivity shown as a solid orange line in Fig. 6 for $m_a \gtrsim 0.5$ meV.

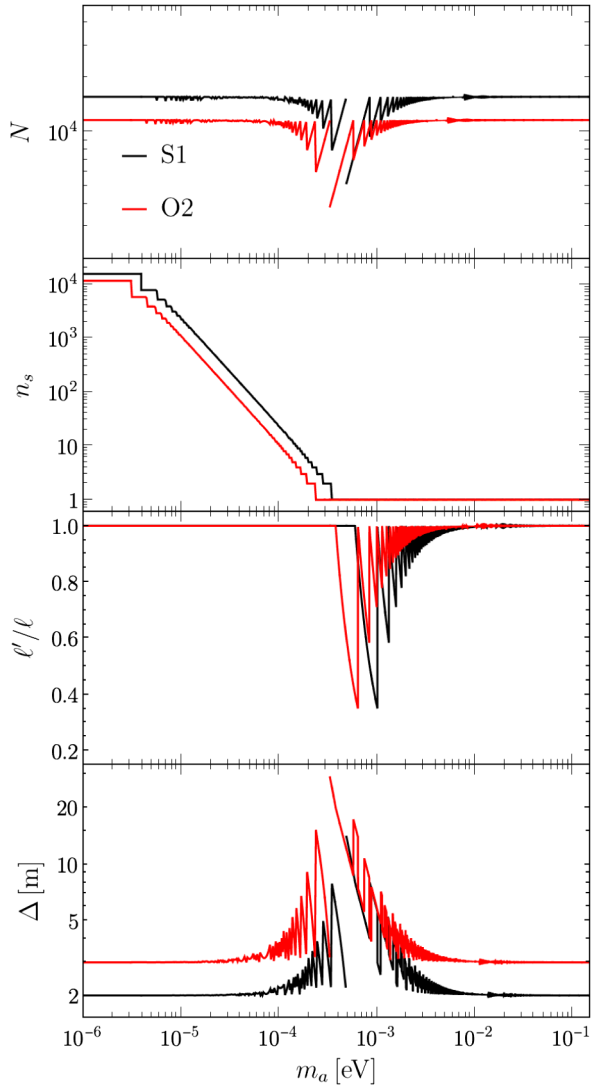

FIG. 7. Optimal parameter choices as a function of m_a for S1 (black) and O2 (red) setups from Table I.

Following the procedure described above, we obtain the optimal values for n_s, n_g, δ, and ℓ' (where $\ell' \neq \ell$ only in the high-mass limit) for each mass m_a to measure the coupling $g_{a\gamma}$ with the desired precision of $\Pi = 2\%$. We show the values of the optimal parameters for the S1 (black line) and O2 (red line) setups in Fig. 7.

APPENDIX C: EXPERIMENTAL COMPONENTS

For reference, we summarize some of the available technology to inform our choices for the HyperLSW benchmark setups and add a number of technical details regarding the clipping losses and filling the experimental setup with a buffer gas.

TABLE II. Overview of proposed or used magnets in other experiments (see also Refs. [126], Sec. 32 and [172]). The value for the aperture diameter a quoted for HERA (ALPS II) magnet corresponds to the lowest among these magnets.

Magnet	B [T]	a [m]	ℓ [m]	Reference(s)
CMS	3.8	6.30	12.5	[173]
FCC-ee (IDEA)	2.0	2.10	6.0	[174]
FCC-hh (MD)	16.0	0.05	15.8	[137]
HERA	4.7	0.07	8.8	[175]
HERA (ALPS II)	5.3	0.09	8.8	[164]
LHC	8.3	0.06	14.3	[176]
MADMAX	9.0	1.35	6.0	[127,128]
TEVATRON	4.4	0.08	6.4	[177]

1. Magnets

In Table II, we list a number of available or proposed magnet designs to extend the selection of magnets available at the time of publication of Ref. [25]. We list the magnetic field strength B, aperture diameter a, and length ℓ. In the main text, we choose a magnet that closely resembles the proposed MADMAX magnet due to its large aperture and sizable magnetic field.

In Fig. 8, we show the sensitivity (as defined in the main text) for various other magnets listed in Table II, using $\Delta_{\rm min} = 0$ for the HERA and LHC magnets and otherwise the parameters for the "S setup" from Table I. Clearly, even without a minimal gap, HERA and LHC magnets cannot probe the QCD axion band, which is due to their small aperture.

2. Optics and clipping losses

As explained in Ref. [25], we have to take into account clipping losses, which effectively limit the total length of the experiment and define its optimal length. To see this, consider the spot size $w(z)$ of a Gaussian beam at distance $z \in [0, z_N]$ with waist size w_0, where $z_N \approx N\ell(1+\delta)$ is the length of one part of the experiment,

$$\frac{w(z)}{w_0} = \sqrt{1 + \left(\frac{z - z_N}{z_{\rm R}}\right)^2}, \tag{C1}$$

with the Rayleigh length $z_{\rm R} = \pi w_0^2 n_{\rm r}/\lambda$. Assuming that the boost factor β is the same in both the generation and regeneration regions ($\beta_{\rm g} = \beta_{\rm r} = \beta$), the sensitivity of the experiment approximately scales with $\beta^{-1/2} L^{-1}$, with β given in Eq. (7). Its maximum for $n_{\rm r} = 1$ is implicitly given by [25]

$$e^{-\zeta}\left(\frac{\zeta}{2} - 1\right) - \beta_0^{-1} = 0, \tag{C2}$$

where $\zeta \equiv \pi a^2/4\lambda z$, a is the aperture (diameter) of the magnets. The quantity $\beta_0^{-1} \equiv -\sum_i \ln(R_i)$ depends on the coefficients R_i, which are reflectivity coefficients related to other losses (mirror transmissivity and imperfections, round trips, etc.).[12]

On the one hand, the approximate solution in Eq. (10) can be obtained by ignoring the term in brackets in Eq. (C2) [25]. On the other hand, the solution can be found numerically. To guarantee the successful convergence of the root finding algorithm, we need to bracket the correct solution, which only exists when $\beta_0 > 2e^3 \approx 40$. Since Eq. (C2) has a maximum at $\zeta = 3$ and, for $\beta_0^{-1} = 0$, a zero at $\zeta = 2$, there should then be a zero in the interval $\zeta \in [2, 3]$. Moreover, for $\zeta \gg 0$, we can approximate Eq. (C2) as $\zeta e^{-\zeta}/2 - \beta_0^{-1}$, which has zeros at $-W_0(-2\beta_0^{-1})$ and $-W_{-1}(-2\beta_0^{-1})$, where W_k denotes the k branch of the Lambert W function. Since $\beta_0 \gtrsim 40$ implies that $-W_0(-2\beta_0^{-1}) \lesssim 0.06$ and $-W_{-1}(-2\beta_0^{-1}) \gtrsim 4.5$, the latter is the only valid solution in the interval $3 < \zeta < -W_{-1}(-2\beta_0^{-1})$, which also leads to the longer experiment.

Choosing $z = z$opt gives a total boost factor that is smaller than the "intrinsic" boost β_0. For the example in Eq. (10), we find $\beta \approx 0.85\beta_0$. Furthermore, Eq. (C2) tells us that larger β_0 leads to lower values of $z_{\rm opt}$. This justifies our simplification for O-type setups in the main text, where we assumed that the total length of the experiment is $2 \times z_{\rm opt}$, where $z_{\rm opt}$ is calculated for the regeneration part of the experiment (ignoring that $\beta_{\rm r} > \beta_{\rm g}$). While the regeneration boost factor is larger, the corresponding cavity contains at

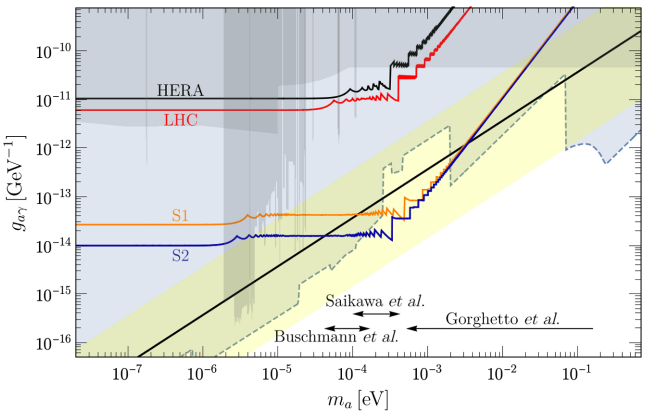

FIG. 8. Sensitivity for LHC (black) and HERA (red) magnets from Table II, consistently compared to the S1 (orange) and S2 (blue) setups from Table I. The QCD axion band (yellow region), KSVZ model (solid black line), various constraints (gray region), and projected haloscope sensitivity (light blue region, dashed line) are also shown (see Fig. 3 for references).

[12]Note that the authors of Ref. [25] define the magnet aperture via its radius, while we use its diameter, implying that Eq. (C2) reduces to Eq. (32) in [25] after replacing $a \to 2a$.

most a small number of photons, drastically reducing heating issues of the mirrors.

3. Buffer gas filling

Filling the LSW setup with a gas changes the refractive index n_r inside the magnetic fields, allowing us to achieve values of $n_\mathrm{r} > 1$. By adjusting n_r we can, in principle, change the momentum transfer q and increase the sensitivity to some m_a values via Eq. (12). The feasibility of this approach has already been demonstrated in a number of LSW experiments [57–59].

A nonoptimal form factor $|F(x)|$ can be improved by shifting its argument, i.e., the phase factor related to the momentum transfer. In Sec. IV D, we shortened the magnet length ℓ to achieve this by shifting to the *previous* maximum of $|F|$. In contrast, a buffer gas with $n_\mathrm{r} > 1$ *increases* the phase difference between the axion and the photon, cf. Eq. (3), and we can thus move to the subsequent maximum. The required shift is

$$\Delta x \sim \pi/2 \Rightarrow \Delta q \ell \approx (n_\mathrm{r} - 1)\omega\ell \sim \pi, \tag{C3}$$

which corresponds to $n_\mathrm{r} - 1 \sim 1.5 \times 10^{-7}$ for the S1 setup.

The value of n_r can be adjusted by changing the pressure via the Lorentz–Lorenz formula (see Ref. [70]),

$$n_\mathrm{r} - 1 = (n_\mathrm{w} - 1)\frac{P_\mathrm{w}}{P_\mathrm{c}}\left(\frac{P_\mathrm{w}}{1\ \mathrm{bar}}\right), \tag{C4}$$

where n_w and P_w are the refractive index and pressure at room temperature, whereas P_c in the pressure inside the cooled LSW setup. For the S1 setup, the required pressure is of order 0.5 mbar, and for the currently ongoing ALPS II experiment, it has been estimated that the round trip losses in the optical cavities due to Rayleigh scattering on He atoms at that pressure are of the order $R = 2 \times 10^{-8}$ [70]. Since a round trip in ALPS II setup has a length of $2L \approx 200$ m [70], an experiment with round trip length $2L = 100$ km would have expected losses of about 500 $R = 10^{-5} \sim \beta_0^{-1}$.

In summary, filling HyperLSW with a buffer gas would at least be challenging, as it already limits the realizable boost factor of the cavity. This is particularly true for the envisioned O-type setup regeneration boost factor of $\beta_\mathrm{r} = 10^6$.

APPENDIX D: EXPERIMENTAL ERRORS

For large m_a, i.e., $y \gtrsim 1/N$, HyperLSW improves the sensitivity of a fully aligned setup by resonantly enhancing the form factor $|F|$ in Eq. (2). This requires accurate magnet placement to achieve gaps of size Δ, which we consider in Appendix D 1. Moreover, $|F|$ depends on the (consistency of the) location and shape $f(z)$ of the magnetic field in Eq. (2), which we consider in Appendix D 2.

1. Magnet positioning errors

One option to arrange HyperLSW is to measure Δ between each pair of magnets. If each measurement has some uncertainty σ_Δ, the positioning error of the last magnet has a (correlated) uncertainty of size $\sqrt{N-1}\sigma_\Delta$. Given the large number of magnets used in HyperLSW, this can be problematic as errors accumulate.

Alternatively, one could measure the absolute position of the magnets and avoid error accumulation. For instance, if satellite navigation systems can be used, we may achieve $\sigma_\Delta = 20$ cm (or better) for the Galileo High Accuracy Service [178]. A surveying station can further improve the satellite navigation error over the course of a few days, which has been demonstrated to give precision of $\sigma_\Delta = 0.7$ cm during construction of the Brenner Base Tunnel [179,180]. Moreover, other advanced surveying techniques exist that should allow absolute positioning relative to fixed points of the setup with an accuracy of $\sigma_\Delta \ll 1$ cm [181].

We can thus reasonably suppose an absolute positioning error of $\sigma_\Delta = 1$ cm for each magnet j, translating into relative offsets $\epsilon_j^\delta \sim \mathcal{N}(0, \sigma_\delta^2)$, where $\sigma_\delta \equiv \sigma_\Delta/\ell$. Starting from Eq. (2) and following Ref. [25], Eq. (19), we find

$$F = \frac{1}{L}\int_0^{(z'_N+\epsilon_N^\delta)\ell} \mathrm{d}z\, f(z)\mathrm{e}^{\mathrm{i}qz} = \frac{1}{N}\int_0^{z'_N+\epsilon_N^\delta} \mathrm{d}z'\, f(z')\mathrm{e}^{2\mathrm{i}xz'} = \frac{1}{N}\sum_{j=1}^{N}\left(\int_{z'_{j-1}}^{z'_j+\epsilon_j^\delta} \mathrm{d}z'\, f(z')\mathrm{e}^{2\mathrm{i}xz'}\right) \tag{D1}$$

$$= \frac{1}{N}\sum_{j=1}^{N}\left[\left(\int_0^1 \mathrm{d}z''_j\, f_{j-1}\,\mathrm{e}^{2\mathrm{i}xz''_j}\right)\mathrm{e}^{2\mathrm{i}x(z'_{j-1}+\epsilon_j^\delta)}\right] = \frac{1}{N}\frac{\mathrm{e}^{2\mathrm{i}x}-1}{2\mathrm{i}x}\sum_{j=1}^{N} f_{j-1}\,\mathrm{e}^{2\mathrm{i}x(z'_{j-1}+\epsilon_j^\delta)} \tag{D2}$$

$$\Rightarrow |F|^2 = \left(\frac{\mathrm{sinc}(x)}{N}\right)^2\left|\sum_{j=0}^{N-1} f_j \mathrm{e}^{2\mathrm{i}x(z'_j+\epsilon_{j+1}^\delta)}\right|^2, \tag{D3}$$

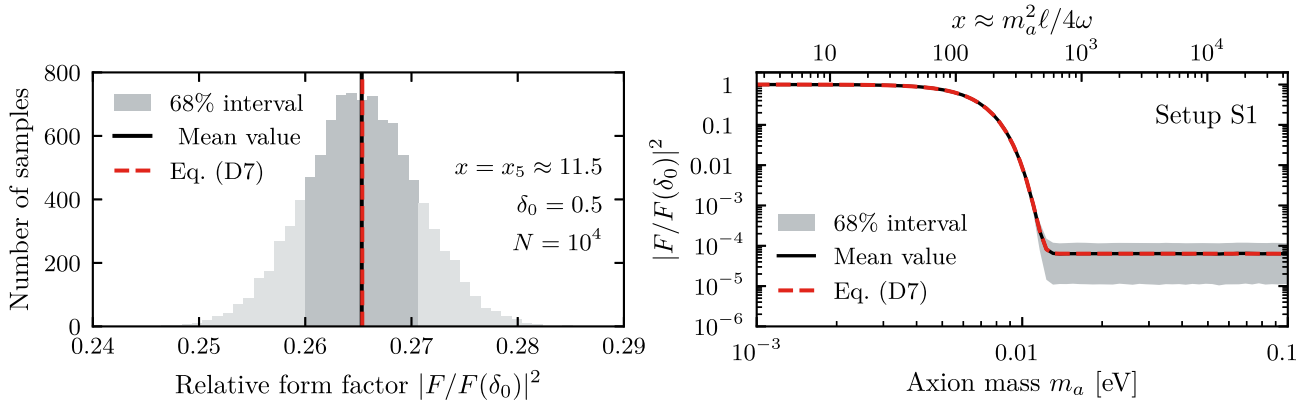

FIG. 9. Form factor uncertainties from positioning errors, based on 10,000 simulations and $\sigma_\Delta = 1$ cm. We show an example distribution for $x = x_5$, $\Delta = 2$ m, and $\ell = 4$ m (left panel) and the uncertainties for the optimized setup S1 across different masses (right panel).

where we defined $z' \equiv z/\ell$, $z'_j \equiv j(1+\delta)$, $z''_j \equiv z' - z'_j$, and used that $f(z') = 0$ in the gaps and $f_j \in \{-1, +1\}$ inside the magnetic fields.[13]

For each half of the experiment, we can compute the effect of positioning uncertainties on $|F|^2$ and thus on the conversion probability, with Monte Carlo (MC) simulations, drawing random values of $\epsilon_j^\delta \sim \mathcal{N}(0, \sigma_\delta^2)$. To better understand the outcome of these computations, consider the most relevant case, the fully alternating setup, i.e., $n_s = 1$ and $f_j = (-1)^j$. For simplicity, further assume that $n_g = N$ is an odd number. Again defining $y \equiv x(1+\delta)$, the expectation value of $|F_{1,N}|^2 = F_{1,N}\bar{F}_{1,N}$ is then given by

$$\frac{\mathrm{E}[|F_{1,N}|^2]}{\mathrm{sinc}^2(x)} = \frac{1}{N^2}\prod_{i=1}^{N}\int \mathrm{d}\epsilon_i^\delta \frac{\mathrm{e}^{-(\epsilon_i^\delta)^2/2\sigma_\delta^2}}{\sqrt{2\pi}\sigma_\delta} \sum_{k,j=0}^{N-1} f_j f_k \, \mathrm{e}^{2\mathrm{i}x[(j-k)(1+\delta)+\epsilon_{j+1}^\delta - \epsilon_{k+1}^\delta]} \tag{D4}$$

$$= \frac{1}{N^2}\left(\sum_{k=0}^{N-1} f_k^2 + \sum_{k,j\neq k} f_k f_j \, \mathrm{e}^{2\mathrm{i}x(j-k)(1+\delta) - 4x^2\sigma_\delta^2}\right) = \frac{1}{N} + \frac{\mathrm{e}^{-4x^2\sigma_\delta^2}}{N^2}\sum_{k,j\neq k}(-1)^{j+k}\,\mathrm{e}^{2\mathrm{i}x(j-k)(1+\delta)} \tag{D5}$$

$$= \frac{1}{N} + \frac{\cos^2(Ny) - N\cos^2(y)}{N^2\cos^2(y)}\mathrm{e}^{-4x^2\sigma_\delta^2} \to \frac{1}{N} + \frac{N-1}{N}\mathrm{e}^{-4x_k^2\sigma_\delta^2} \quad (x \to x_k). \tag{D6}$$

Equation (D6) shows that the random placement errors will introduce a systematic shift in the estimate, which becomes more significant at larger x. There are also statistical fluctuations, but we do not perform the related, rather involved computation of $\mathrm{Var}[|F_{1,N}|^2]$. Also note that $\mathrm{E}[|F_{1,N}|^2] \to \mathrm{sinc}^2(x)\cos^2(Ny)/N^2\cos^2(y)$ for $\sigma_\delta \to 0$, in agreement with Eq. (4).

Figure 9 shows an example for the ensuing distribution for $x = x_5 \approx 11.5$ (left panel) and the effect of uncertainties for the optimal parameters in our proposed setup S1 across the entire m_a range (right panel). In both cases, we assume that $\sigma_\Delta = 1$ cm and perform 10,000 MC simulations for each configuration.

In particular, for values of $m_a \gtrsim 4$ meV, the positioning uncertainties cause a significant shift in the expectation value of more than 10% (plus sizable scatter) in the form factor and thus in the expected number of counts. This is not entirely surprising since only the high-mass region strongly depends on resonant enhancement and thus requires an accurately positioned experimental setup. In any case, we can compute the impact of the positioning uncertainties and, even for a conservative value of $\sigma_\Delta = 1$ cm, they would only affect the multi-meV mass region.

[13]For relative distance measurements, replace $\epsilon_j \mapsto \sum_{k=1}^{j}\epsilon_k$.

2. Realistic magnetic field profiles

HyperLSW likely requires thousands of magnets, and we thus have to assume that the magnet profiles $f(z)$ will be subject to production errors such as asymmetries and length variations. Moreover, $f(z)$ will not have the top-hat profile that we assume in the main text, but smoothly decreases outside of the nominal "iron length" ℓ.

There is a variety of functions to describe such a behavior and, for computational efficiency, we choose the "smooth(er) step" functions $\mathrm{smst}(z; a_1, a_2)$ [182], which define a step between $a_1 < a_2$ such that the function vanishes for $z < a_1$ and is unity for $z > a_2$. This allows us to construct smooth top hat between $-\zeta < z < 1 + \epsilon^\ell + \zeta$, where $\zeta > 0$ defines the size of the smooth step, and ϵ^ℓ is a small shift in the magnetic field length (both in units of ℓ). The magnetic form factors $f_j(z')$ are then given by

$$f_j(z') = f_j \mathrm{smst}(z' + \epsilon^\zeta; -\zeta, 0)\,\mathrm{smst}(-z' - \epsilon^\zeta; -1 - \epsilon^\ell - \zeta, -1 - \epsilon^\ell), \tag{D7}$$

$$\text{with} \quad \mathrm{smst}(z; a_1, a_2) = \frac{(z-a_1)^3(6z^2 + 3za_1 + a_1^2 - 5(3z + a_1)a_2 + 10a_2^2)}{(a_2 - a_1)^5}\Theta(z - a_1)\Theta(a_2 - z) + \Theta(z - a_2), \tag{D8}$$

where $f_j \in \{-1, +1\}$ and where ϵ^ζ is a small offset (in units of ℓ) from the magnetic field center. We can then follow the derivation in Appendix D 1, defining $z_j'' = z' - z_j'$ with $z_j' = j(1+\delta) + \sum_{k=1}^{j}(\epsilon_k^\ell + \epsilon_k^\zeta)$ and $\widetilde{\ell}_j \equiv 1 + \epsilon_j^\ell + \zeta$ to find

$$F = \frac{1}{N}\int_{-\zeta}^{z_N' + \zeta + \sum_k \epsilon_k^\ell} \mathrm{d}z' f(z') \mathrm{e}^{2\mathrm{i}xz'} = \frac{1}{N}\sum_{j=1}^{N}\left[\left(\int_{-\zeta}^{1+\epsilon_j^\ell+\zeta} \mathrm{d}z_j''\, f(z_j'')\, \mathrm{e}^{2\mathrm{i}xz_j''}\right)\mathrm{e}^{2\mathrm{i}xz_{j-1}'}\right], \tag{D9}$$

$$\text{where} \int_{-\zeta}^{1+\epsilon_j^\ell+\zeta} \mathrm{d}z'' f(z'')\mathrm{e}^{2\mathrm{i}xz''} = f_j \frac{15(3 - \zeta^2x^2)\mathrm{sinc}(\zeta x) - 3\cos(\zeta x)}{\zeta^4 x^4}\widetilde{\ell}_j \mathrm{sinc}(\widetilde{\ell}_j x)\mathrm{e}^{\mathrm{i}x(1+\epsilon_j^\ell)} \tag{D10}$$

$$\simeq f_j \widetilde{\ell}_j\, \mathrm{sinc}(\widetilde{\ell}_j x)\mathrm{e}^{\mathrm{i}x(1+\epsilon_j^\ell)} \quad (\zeta x \to 0). \tag{D11}$$

For $\epsilon^\zeta = 0$, we can absorb the effect of the smoother profile into a multiplicative factor, i.e., into an effective magnetic field strength. For $\epsilon^\ell = 0$, and in the limit of $x \to 0$, this factor is $\sqrt{1+\zeta} > 1$, and we denote magnitude of the associated form factor with F_{eff}.

Based on experience from the LHC, the systematic differences for ϵ^ℓ between manufacturers were 14 mm, while the intrinsic scatter for each manufacturer was less than 3 mm [183]. We use these findings to define the typical uncertainty and simulate the proposed HyperLSW configuration for setup S1 with $\epsilon_j^\ell \sim \mathcal{N}(0, \sigma_\ell^2)$ and $\epsilon_j^\zeta \sim \mathcal{N}(0, \sigma_\zeta^2)$, where we choose σ_ℓ and σ_ζ to both correspond to absolute values of 1 cm.

To estimate ζ, we use a publicly available simulation for the magnetic field profile of the upcoming IAXO experiment [159–161], which is available in Ref. [184]. The magnet has an "iron length" of $\ell = 6.7$ m and an aperture diameter of $a = 0.7$ m, and we find a best-fitting value for smooth step of around $\zeta = 0.35$. In fact, the relevant quantity that sets the size of ζ is a, as has been established by the expansion of fringe fields, with $\zeta = \eta_\zeta\, a/\ell$ and $\eta_\zeta \sim 4$–5, e.g., Ref. [185], Fig. 3 (see also Ref. [186]). This is in line with the simulated IAXO magnet, where $\zeta = 3.5a/\ell$. If we used the same relation for the magnetic in setup S1, we would have $\zeta = 1.1$, and since $\delta = 0.5$, there would be a significant overlap between the stray fields of two consecutive magnets. To simplify the computation, we choose $\zeta = 0.2$.

We again perform 10,000 MC simulations for each configuration of the optimized S1 setup, assuming the uncertainties listed above. We also again include an example distribution as the left panel of Fig. 10, which shows that the accumulating, correlated errors, although small, can lead to highly asymmetric distributions of $|F|^2$. Note that we normalized the results with respect to the ideal, effective form factor Feff at low m_a, i.e., without uncertainties.

In the right panel of Fig. 10, we find both a systematic shift and scatter in the distribution of $|F|^2$, which is the same qualitatively similar to what we observed for the positioning errors in Appendix D 1. These effects are most pronounced at larger m_a, again due to the resonant enhancement, which requires an accurately arranged setup. For the choice of uncertainties considered, the expected $|F|^2$ sees a shift of more than 10% for $m_a \gtrsim 0.6$ meV. At $m_a \gtrsim 10$ meV, note that the figure might show some computational issues due to numerical cancellation effects.

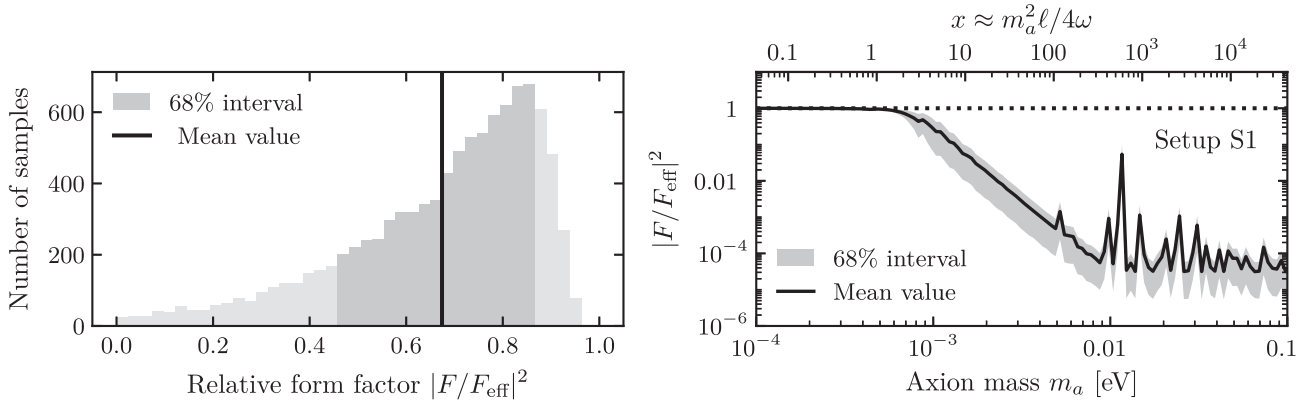

FIG. 10. Effects of magnetic field profile uncertainties on the form factor, based on 10,000 simulations and $\sigma_\ell \ell = \sigma_\zeta \ell = 1$ cm. We show an example distribution for $x = x_5$, $\Delta = 2$ m, and $\ell = 4$ m (left panel) and the uncertainties for our optimized setup S1 across different masses (right panel).

However, it is clear that, for those masses, the magnetic field profile uncertainties will be an issues. Again, lower uncertainties will improve this situation, while individually measured magnetic field could allow us to ameliorate these issues by suitably arranging the magnets or gaps to compensate for the variation in magnetic field profiles.

[1] F. Wilczek, Problem of strong$P$ and T invariance in the presence of instantons, Phys. Rev. Lett. **40**, 279 (1978).
[2] S. Weinberg, A new light boson?, Phys. Rev. Lett. **40**, 223 (1978).
[3] J. E. Kim, Light pseudoscalars, particle physics and cosmology, Phys. Rep. **150**, 1 (1987).
[4] J. Jaeckel and A. Ringwald, The low-energy frontier of particle physics, Annu. Rev. Nucl. Part. Sci. **60**, 405 (2010).
[5] R. D. Peccei and H. R. Quinn, CP conservation in the presence of pseudoparticles, Phys. Rev. Lett. **38**, 1440 (1977).
[6] R. D. Peccei and H. R. Quinn, Constraints imposed by CP conservation in the presence of pseudoparticles, Phys. Rev. D **16**, 1791 (1977).
[7] J. Preskill, M. B. Wise, and F. Wilczek, Cosmology of the invisible axion, Phys. Lett. **120B**, 127 (1983).
[8] L. F. Abbott and P. Sikivie, A cosmological bound on the invisible axion, Phys. Lett. **120B**, 133 (1983).
[9] M. Dine and W. Fischler, The not-so-harmless axion, Phys. Lett. **120B**, 137 (1983).
[10] M. S. Turner, Coherent scalar-field oscillations in an expanding universe, Phys. Rev. D **28**, 1243 (1983).
[11] M. S. Turner, Cosmic and local mass density of, "invisible" axions, Phys. Rev. D **33**, 889 (1986).
[12] P. Arias, D. Cadamuro, M. Goodsell, J. Jaeckel, J. Redondo, and A. Ringwald, WISPy cold dark matter, J. Cosmol. Astropart. Phys. 06 (2012) 013.
[13] I. G. Irastorza and J. Redondo, New experimental approaches in the search for axion-like particles, Prog. Part. Nucl. Phys. **102**, 89 (2018).
[14] L. Di Luzio, M. Giannotti, E. Nardi, and L. Visinelli, Corrigendum to "The landscape of QCD axion models" [Phys. Rep. 870 (2020) 1–117], Phys. Rep. **870**, 1 (2020).
[15] P. Sikivie, Experimental tests of the, "invisible" axion, Phys. Rev. Lett. **51**, 1415 (1983).
[16] V. Dandoy, J. Jaeckel, and V. Montoya, Using axion miniclusters to disentangle the axion-photon coupling and the dark matter density, J. Cosmol. Astropart. Phys. 05 (2024) 035.
[17] J. Jaeckel and L. J. Thormaehlen, Distinguishing axion models with IAXO, J. Cosmol. Astropart. Phys. 03 (2019) 039.
[18] T. Dafni, C. A. J. O'Hare, B. Lakić, J. Galán, F. J. Iguaz, I. G. Irastorza, K. Jakovčić, G. Luzón, J. Redondo, and E. Ruiz Chóliz, Weighing the solar axion, Phys. Rev. D **99**, 035037 (2019).
[19] A. A. Anselm, Arion ↔ photon oscillations in a steady magnetic field. (In Russian), Yad. Fiz. **42**, 1480 (1985).
[20] K. van Bibber, N. R. Dagdeviren, S. E. Koonin, A. K. Kerman, and H. N. Nelson, Proposed experiment to produce and detect light pseudoscalars, Phys. Rev. Lett. **59**, 759 (1987).
[21] A. Arvanitaki and A. A. Geraci, Resonantly detecting axion-mediated forces with nuclear magnetic resonance, Phys. Rev. Lett. **113**, 161801 (2014).

[22] C. A. J. O'Hare and E. Vitagliano, Cornering the axion with *CP*-violating interactions, Phys. Rev. D **102**, 115026 (2020).
[23] P. W. Graham, I. G. Irastorza, S. K. Lamoreaux, A. Lindner, and K. A. van Bibber, Experimental searches for the axion and axion-like particles, Annu. Rev. Nucl. Part. Sci. **65**, 485 (2015).
[24] C. B. Adams, N. Aggarwal, A. Agrawal, R. Balafendiev, C. Bartram, M. Baryakhtar *et al.*, Axion dark matter, arXiv:2203.14923.
[25] P. Arias, J. Jaeckel, J. Redondo, and A. Ringwald, Optimizing light-shining-through-a-wall experiments for axion and other weakly interacting slim particle searches, Phys. Rev. D **82**, 115018 (2010).
[26] S. De Panfilis, A. C. Melissinos, B. E. Moskowitz, J. T. Rogers, Y. K. Semertzidis, W. U. Wuensch, H. J. Halama, A. G. Prodell, W. B. Fowler, and F. A. Nezrick, Limits on the abundance and coupling of cosmic axions at $4.5 < m_a < 5.0$ μeV, Phys. Rev. Lett. **59**, 839 (1987).
[27] C. Hagmann, P. Sikivie, N. S. Sullivan, and D. B. Tanner, Results from a search for cosmic axions, Phys. Rev. D **42**, 1297 (1990).
[28] S. J. Asztalos, R. F. Bradley, L. Duffy, C. Hagmann, D. Kinion, D. M. Moltz *et al.*, Improved Rf cavity search for halo axions, Phys. Rev. D **69**, 011101 (2004).
[29] S. J. Asztalos, G. Carosi, C. Hagmann, D. Kinion, K. van Bibber, M. Hotz *et al.*, SQUID-based microwave cavity search for dark-matter axions, Phys. Rev. Lett. **104**, 041301 (2010).
[30] N. Du, N. Force, R. Khatiwada, E. Lentz, R. Ottens, L. J. Rosenberg *et al.*, Search for invisible axion dark matter with the axion dark matter experiment, Phys. Rev. Lett. **120**, 151301 (2018).
[31] T. Braine, R. Cervantes, N. Crisosto, N. Du, S. Kimes, L. J. Rosenberg *et al.*, Extended search for the invisible axion with the axion dark matter experiment, Phys. Rev. Lett. **124**, 101303 (2020).
[32] ADMX Collaboration, C. Bartram, T. Braine, E. Burns, R. Cervantes, N. Crisosto *et al.*, Search for "invisible" axion dark matter in the $3.3 - 4.2$ μeV mass range, Phys. Rev. Lett. **127**, 261803 (2021).
[33] S. Lee, S. Ahn, J. Choi, B. R. Ko, and Y. K. Semertzidis, Axion dark matter search around 6.7 μeV, Phys. Rev. Lett. **124**, 101802 (2020).
[34] J. Jeong, S. Youn, S. Bae, J. Kim, T. Seong, J. E. Kim, and Y. K. Semertzidis, Search for invisible axion dark matter with a multiple-cell haloscope, Phys. Rev. Lett. **125**, 221302 (2020).
[35] O. Kwon, D. Lee, W. Chung, D. Ahn, H. Byun, F. Caspers *et al.*, First results from an axion haloscope at CAPP around 10.7 μeV, Phys. Rev. Lett. **126**, 191802 (2021).
[36] Y. Lee, B. Yang, H. Yoon, M. Ahn, H. Park, B. Min, D. Kim, and J. Yoo, Searching for invisible axion dark matter with an 18 T magnet haloscope, Phys. Rev. Lett. **128**, 241805 (2022).
[37] J. Kim, O. Kwon, Ç. Kutlu, W. Chung, A. Matlashov, S. Uchaikin *et al.*, Near-quantum-noise axion dark matter search at CAPP around 9.5 μeV, Phys. Rev. Lett. **130**, 091602 (2023).
[38] A. K. Yi, S. Ahn, Ç. Kutlu, J. Kim, B. R. Ko, B. I. Ivanov *et al.*, Axion dark matter search around 4.55 μeV with Dine-Fischler-Srednicki-Zhitnitskii sensitivity, Phys. Rev. Lett. **130**, 071002 (2023).
[39] B. Yang, H. Yoon, M. Ahn, Y. Lee, and J. Yoo, Extended axion dark matter search using the CAPP18T haloscope, Phys. Rev. Lett. **131**, 081801 (2023).
[40] B. T. McAllister, G. Flower, E. N. Ivanov, M. Goryachev, J. Bourhill, and M. E. Tobar, The ORGAN experiment: An axion haloscope above 15 GHz, Phys. Dark Universe **18**, 67 (2017).
[41] L. Zhong, S. Al Kenany, K. M. Backes, B. M. Brubaker, S. B. Cahn, G. Carosi *et al.*, Results from phase 1 of the HAYSTAC microwave cavity axion experiment, Phys. Rev. D **97**, 092001 (2018).
[42] D. Alesini, C. Braggio, G. Carugno, N. Crescini, D. D'Agostino, D. Di Gioacchino *et al.*, Galactic axions search with a superconducting resonant cavity, Phys. Rev. D **99**, 101101 (2019).
[43] K. M. Backes, D. A. Palken, S. A. Kenany, B. M. Brubaker, S. B. Cahn, A. Droster *et al.*, A quantum enhanced search for dark matter axions, Nature (London) **590**, 238 (2021).
[44] D. Alesini, C. Braggio, G. Carugno, N. Crescini, D. D'Agostino, D. Di Gioacchino *et al.*, Search for invisible axion dark matter of mass $m_a = 43$ μeV with the QUAX-a γ experiment, Phys. Rev. D **103**, 102004 (2021).
[45] A. Álvarez Melcón, S. Arguedas Cuendis, J. Baier, K. Barth, H. Bräuninger, S. Calatroni *et al.*, First results of the CAST-RADES haloscope search for axions at 34.67 μeV, J. High Energy Phys. 10 (2021) 075.
[46] T. Grenet, R. Ballou, Q. Basto, K. Martineau, P. Perrier, P. Pugnat *et al.*, The grenoble axion haloscope platform (GrAHal): Development plan and first results, arXiv:2110.14406.
[47] C. M. Adair, K. Altenmüller, V. Anastassopoulos, S. Arguedas Cuendis, J. Baier, K. Barth *et al.*, Search for dark matter axions with CAST-CAPP, Nat. Commun. **13**, 6180 (2022).
[48] A. P. Quiskamp, B. T. McAllister, P. Altin, E. N. Ivanov, M. Goryachev, and M. E. Tobar, Direct search for dark matter axions excluding ALP cogenesis in the 63-67 micro-eV range, with The ORGAN experiment, Sci. Adv. **8**, abq3765 (2022).
[49] H. Chang, J.-Y. Chang, Y.-C. Chang, Y.-H. Chang, Y.-H. Chang, C.-H. Chen *et al.*, First results from the Taiwan axion search experiment with a haloscope at 19.6 μeV, Phys. Rev. Lett. **129**, 111802 (2022).
[50] D. Alesini, D. Babusci, C. Braggio, G. Carugno, N. Crescini, D. D'Agostino *et al.*, Search for Galactic axions with a high-Q dielectric cavity, Phys. Rev. D **106**, 052007 (2022).
[51] M. J. Jewell, A. F. Leder, K. M. Backes, X. Bai, K. van Bibber *et al.* (HAYSTAC Collaboration), New results from HAYSTAC's phase II operation with a squeezed state receiver, Phys. Rev. D **107**, 072007 (2023).
[52] C. A. J. O'Hare and A. M. Green, Axion astronomy with microwave cavity experiments, Phys. Rev. D **95**, 063017 (2017).

[53] J. W. Foster, N. L. Rodd, and B. R. Safdi, Revealing the dark matter halo with axion direct detection, Phys. Rev. D **97**, 123006 (2018).
[54] S. Knirck, A. J. Millar, C. A. J. O'Hare, J. Redondo, and F. D. Steffen, Directional axion detection, J. Cosmol. Astropart. Phys. 11 (2018) 051.
[55] C. A. J. O'Hare, G. Pierobon, and J. Redondo, Axion minicluster streams in the solar neighbourhood, Phys. Rev. Lett. **133**, 081001 (2024).
[56] K. Ehret, M. Frede, S. Ghazaryan, M. Hildebrandt, E.-A. Knabbe, D. Kracht *et al.*, Resonant laser power build-up in ALPS—A "light shining through a wall" experiment, Nucl. Instrum. Methods Phys. Res., Sect. A **612**, 83 (2009).
[57] K. Ehret, M. Frede, S. Ghazaryan, M. Hildebrandt, E.-A. Knabbe, D. Kracht *et al.*, New ALPS results on hidden-sector lightweights, Phys. Lett. B **689**, 149 (2010).
[58] P. Pugnat, L. Duvillaret, R. Jost, G. Vitrant, D. Romanini, A. Siemko *et al.*, Results from the OSQAR photon-regeneration experiment: No light shining through a wall, Phys. Rev. D **78**, 092003 (2008).
[59] M. Schott, P. Pugnat, R. Ballou, L. Duvillaret, T. Husek, R. Jost *et al.*, First results of the full-scale OSQAR photon regeneration experiment, arXiv:1110.0774.
[60] R. Ballou, G. Deferne, M. Finger, M. Finger, L. Flekova, J. Hosek *et al.*, New exclusion limits on scalar and pseudoscalar axionlike particles from light shining through a wall, Phys. Rev. D **92**, 092002 (2015).
[61] G. Ruoso, R. Cameron, G. Cantatore, A. C. Melissinos, Y. Semertzidis, H. J. Halama *et al.*, Search for photon regeneration in a magnetic field, Z. Phys. C **56**, 505 (1992).
[62] R. Cameron, G. Cantatore, A. C. Melissinos, G. Ruoso, Y. Semertzidis, H. J. Halama *et al.*, Search for nearly massless, weakly coupled particles by optical techniques, Phys. Rev. D **47**, 3707 (1993).
[63] A. V. Afanasev, O. K. Baker, K. W. McFarlane, G. H. Biallas, J. R. Boyce, and M. D. Shinn, Production and detection of very light spin-zero bosons at optical frequencies, arXiv:hep-ph/0605250.
[64] C. Robilliard, R. Battesti, M. Fouché, J. Mauchain, A. M. Sautivet, F. Amiranoff, and C. Rizzo, No "light shining through a wall": Results from a photoregeneration experiment, Phys. Rev. Lett. **99**, 190403 (2007).
[65] A. S. Chou, W. Wester, A. Baumbaugh, H. R. Gustafson, Y. Irizarry-Valle, P. O. Mazur, J. H. Steffen, R. Tomlin, X. Yang, and J. Yoo, Search for axionlike particles using a variable-baseline photon-regeneration technique, Phys. Rev. Lett. **100**, 080402 (2008).
[66] A. Afanasev, O. K. Baker, K. B. Beard, G. Biallas, J. Boyce, M. Minarni, R. Ramdon, M. Shinn, and P. Slocum, Experimental limit on optical-photon coupling to light neutral scalar bosons, Phys. Rev. Lett. **101**, 120401 (2008).
[67] M. Betz, F. Caspers, M. Gasior, M. Thumm, and S. W. Rieger, First results of the CERN resonant WISP search (CROWS), Phys. Rev. D **88**, 075014 (2013).
[68] F. Della Valle, A. Ejlli, U. Gastaldi, G. Messineo, E. Milotti, R. Pengo, G. Ruoso, and G. Zavattini, The PVLAS experiment: Measuring vacuum magnetic birefringence and dichroism with a birefringent Fabry-Perot cavity, Eur. Phys. J. C **76**, 24 (2016).
[69] J. Redondo and A. Ringwald, Light shining through walls, Contemp. Phys. **52**, 211 (2011).
[70] R. Bähre, B. Döbrich, J. Dreyling-Eschweiler, S. Ghazaryan, R. Hodajerdi, D. Horns *et al.*, Any light particle search II—Technical design report, J. Instrum. **8**, T09001 (2013).
[71] F. Hoogeveen and T. Ziegenhagen, Production and detection of light bosons using optical resonators, Nucl. Phys. **B358**, 3 (1991).
[72] G. Mueller, P. Sikivie, D. B. Tanner, and K. van Bibber, Detailed design of a resonantly enhanced axion-photon regeneration experiment, Phys. Rev. D **80**, 072004 (2009).
[73] J. Jaeckel and A. Ringwald, Extending the reach of axion photon regeneration experiments towards larger masses with phase shift plates, Phys. Lett. B **653**, 167 (2007).
[74] R. Janish, V. Narayan, S. Rajendran, and P. Riggins, Axion production and detection with superconducting Rf cavities, Phys. Rev. D **100**, 015036 (2019).
[75] M. Zarei, S. Shakeri, M. Sharifian, M. Abdi, D. J. E. Marsh, and S. Matarrese, Probing virtual axion-like particles by precision phase measurements, J. Cosmol. Astropart. Phys. 06 (2022) 012.
[76] M. Sharifian, M. Zarei, M. Abdi, M. Peloso, and S. Matarrese, Probing virtual ALPs by precision phase measurements: Time-varying magnetic field background, J. Cosmol. Astropart. Phys. 04 (2023) 036.
[77] H. Seong, C. Sun, and S. Yun, Axion magnetic resonance: A novel enhancement in axion-photon conversion, Phys. Rev. D **110**, 015018 (2024).
[78] Wikipedia Contributors, Mponeng gold mine—Wikipedia, the free encyclopedia, https://en.wikipedia.org/w/index.php?title=Mponeng_Gold_Mine&oldid=1229726145 (2024) [Online; accessed 26-June-2024].
[79] G. Cowan, K. Cranmer, E. Gross, and O. Vitells, Asymptotic formulae for likelihood-based tests of new physics, Eur. Phys. J. C **71**, 1554 (2011).
[80] G. G. di Cortona, E. Hardy, J. P. Vega, and G. Villadoro, The QCD axion, precisely, J. High Energy Phys. 01 (2016) 034.
[81] J. E. Kim, Weak-interaction singlet and strong*CP* invariance, Phys. Rev. Lett. **43**, 103 (1979).
[82] M. A. Shifman, A. I. Vainshtein, and V. I. Zakharov, Can confinement ensure natural *CP* invariance of strong interactions?, Nucl. Phys. **B166**, 493 (1980).
[83] V. Plakkot and S. Hoof, Anomaly ratio distributions of hadronic axion models with multiple heavy quarks, Phys. Rev. D **104**, 075017 (2021).
[84] J. Diehl and E. Koutsangelas, Dine-Fischler-Srednicki-Zhitnitsky-type axions and where to find them, Phys. Rev. D **107**, 095020 (2023).
[85] L. Di Luzio, F. Mescia, and E. Nardi, Redefining the axion window, Phys. Rev. Lett. **118**, 031801 (2017).
[86] L. Di Luzio, F. Mescia, and E. Nardi, Window for preferred axion models, Phys. Rev. D **96**, 075003 (2017).
[87] A. R. Zhitnitsky, On possible suppression of the axion hadron interactions, Sov. J. Nucl. Phys. **31**, 260 (1980).

[88] M. Dine, W. Fischler, and M. Srednicki, A simple solution to the strong *CP* problem with a harmless axion, Phys. Lett. **104B**, 199 (1981).
[89] J. Diehl and E. Koutsangelas, DFSZ axions and where to find them, Available on Zenodo at 10.5281/zenodo.7656939 (2023).
[90] A. Sonnenschein, BREAD: Broadband reflector experiment for axion detection, in *CPAD Instrumentation Frontier Workshop* (2021), https://indico.fnal.gov/event/46746/contributions/210242/attachments/141320/177905/BREAD_CPAD_2021.pdf.
[91] J. I. Read, The local dark matter density, J. Phys. G **41**, 063101 (2014).
[92] P. F. de Salas and A. Widmark, Dark matter local density determination: Recent observations and future prospects, Rep. Prog. Phys. **84**, 104901 (2021).
[93] W. U. Wuensch, S. de Panfilis-Wuensch, Y. K. Semertzidis, J. T. Rogers, A. C. Melissinos, H. J. Halama, B. E. Moskowitz, A. G. Prodell, W. B. Fowler, and F. A. Nezrick, Results of a laboratory search for cosmic axions and other weakly coupled light particles, Phys. Rev. D **40**, 3153 (1989).
[94] C. Hagmann, D. Kinion, W. Stoeffl, K. van Bibber, E. Daw, J. McBride *et al.*, First results from a second generation galactic axion experiment, Nucl. Phys. B, Proc. Suppl. **51**, 209 (1996).
[95] A. Ayala, I. Domínguez, M. Giannotti, A. Mirizzi, and O. Straniero, Revisiting the bound on axion-photon coupling from globular clusters, Phys. Rev. Lett. **113**, 191302 (2014).
[96] C. Boutan, M. Jones, B. H. LaRoque, N. S. Oblath, R. Cervantes, N. Du *et al.*, Piezoelectrically tuned multimode cavity search for axion dark matter, Phys. Rev. Lett. **121**, 261302 (2018).
[97] N. Crisosto, P. Sikivie, N. S. Sullivan, D. B. Tanner, J. Yang, and G. Rybka, ADMX SLIC: Results from a superconducting LC circuit investigating cold axions, Phys. Rev. Lett. **124**, 241101 (2020).
[98] C. Bartram, T. Braine, R. Cervantes, N. Crisosto, N. Du, G. Leum *et al.*, Dark matter axion search using a Josephson traveling wave parametric amplifier, Rev. Sci. Instrum. **94**, 044703 (2023).
[99] H. Yoon, M. Ahn, B. Yang, Y. Lee, D. Kim, H. Park, B. Min, and J. Yoo, Axion haloscope using an 18 T high temperature superconducting magnet, Phys. Rev. D **106**, 092007 (2022).
[100] M. J. Dolan, F. J. Hiskens, and R. R. Volkas, Advancing globular cluster constraints on the axion-photon coupling, J. Cosmol. Astropart. Phys. 10 (2022) 096.
[101] D. Noordhuis, A. Prabhu, S. J. Witte, A. Y. Chen, F. Cruz, and C. Weniger, Novel constraints on axions produced in pulsar polar-cap cascades, Phys. Rev. Lett. **131**, 111004 (2023).
[102] R. Di Vora, A. Lombardi, A. Ortolan, R. Pengo, G. Ruoso, C. Braggio *et al.*, Search for galactic axions with a traveling wave parametric amplifier, Phys. Rev. D **108**, 062005 (2023).
[103] D. Alesini, D. Babusci, P. Beltrame, F. Bossi, P. Ciambrone, A. D'Elia *et al.*, The future search for low-frequency axions and new physics with the FLASH resonant cavity experiment at Frascati National Laboratories, Phys. Dark Universe **42**, 101370 (2023).
[104] A. Quiskamp, B. T. McAllister, P. Altin, E. N. Ivanov, M. Goryachev, and M. E. Tobar, Exclusion of axionlike-particle cogenesis dark matter in a mass window above 100 μeV, Phys. Rev. Lett. **132**, 031601 (2024).
[105] Y. Kim, J. Jeong, S. Youn, S. Bae, K. Lee, A. F. van Loo *et al.*, Experimental search for invisible axions as a test of axion cosmology around 22 ueV, Phys. Rev. Lett. **133**, 051802 (2024).
[106] S. Ahn, J. Kim, B. I. Ivanov, O. Kwon, H. Byun, A. F. van Loo *et al.*, Extensive search for axion dark matter over 1 GHz with CAPP's Main Axion eXperiment, Phys. Rev. X **14**, 031023 (2024).
[107] S. Ahyoune, A. Álvarez Melcón, S. Arguedas Cuendis, S. Calatroni, C. Cogollos, A. Díaz-Morcillo *et al.*, RADES axion search results with a high-temperature superconducting cavity in an 11.7 T magnet, arXiv:2403.07790.
[108] C. A. Manzari, Y. Park, B. R. Safdi, and I. Savoray, Supernova axions convert to gamma-rays in magnetic fields of progenitor stars, Phys. Rev. Lett. **133**, 211002 (2024).
[109] I. Stern and On behalf of the ADMX experiment, ADMX status, Proc. Sci. ICHEP2016 (**2016**) 198.
[110] M. Baryakhtar, J. Huang, and R. Lasenby, Axion and hidden photon dark matter detection with multilayer optical haloscopes, Phys. Rev. D **98**, 035006 (2018).
[111] M. Lawson, A. J. Millar, M. Pancaldi, E. Vitagliano, and F. Wilczek, Tunable axion plasma haloscopes, Phys. Rev. Lett. **123**, 141802 (2019).
[112] S. Beurthey, N. Böhmer, P. Brun, A. Caldwell, L. Chevalier, C. Diaconu *et al.*, MADMAX status report, arXiv:2003.10894.
[113] J. Liu, K. Dona, G. Hoshino, S. Knirck, N. Kurinsky, M. Malaker *et al.*, Broadband solenoidal haloscope for terahertz axion detection, Phys. Rev. Lett. **128**, 131801 (2022).
[114] L. Brouwer, S. Chaudhuri, H. M. Cho, J. Corbin, W. Craddock, C. S. Dawson *et al.*, Projected sensitivity of DMRadio-m^3: A search for the QCD axion below 1 μeV, Phys. Rev. D **106**, 103008 (2022).
[115] B. Aja, S. Arguedas Cuendis, I. Arregui, E. Artal, R. Belén Barreiro, F. J. Casas *et al.*, The canfranc axion detection experiment (CADEx): Search for axions at 90 GHz with kinetic inductance detectors, J. Cosmol. Astropart. Phys. 11 (2022) 044.
[116] J. De Miguel, J. F. Hernández-Cabrera, E. Hernández-Suárez, E. Joven-Álvarez, C. Otani, and J. Alberto Rubiño-Martín, Discovery prospects with the dark-photons & axion-like particles interferometer, Phys. Rev. D **109**, 062002 (2024).
[117] F. Bajjali, S. Dornbusch, M. Ekmedžić, D. Horns, C. Kasemann, A. Lobanov *et al.*, First results from BRASS-p broadband searches for hidden photon dark matter, J. Cosmol. Astropart. Phys. 08 (2023) 077.
[118] S. Ahyoune, A. Álvarez Melcón, S. Arguedas Cuendis, S. Calatroni, C. Cogollos, J. Devlin *et al.*, A proposal for a lowfrequency axion search in the $1-2$ μu eV range and

below with the BabyIAXO magnet, Ann. Phys. (Berlin) **535**, 2300326 (2023).
[119] C. O'Hare, cajohare/axionlimits: Axionlimits, Available on Github at https://cajohare.github.io/AxionLimits/ (2020).
[120] M. Gorghetto, E. Hardy, and G. Villadoro, Axions from strings: The attractive solution, J. High Energy Phys. 07 (2018) 151.
[121] M. Buschmann, J. W. Foster, and B. R. Safdi, Early-universe simulations of the cosmological axion, Phys. Rev. Lett. **124**, 161103 (2020).
[122] M. Buschmann, J. W. Foster, A. Hook, A. Peterson, D. E. Willcox, W. Zhang, and B. R. Safdi, Dark matter from axion strings with adaptive mesh refinement, Nat. Commun. **13**, 1049 (2022).
[123] M. Gorghetto, E. Hardy, and G. Villadoro, More axions from strings, SciPost Phys. **10**, 050 (2021).
[124] K. Saikawa, J. Redondo, A. Vaquero, and M. Kaltschmidt, Spectrum of global string networks and the axion dark matter mass, J. Cosmol. Astropart. Phys. 10 (2024) 043.
[125] F. D'Eramo, E. Di Valentino, W. Giarè, F. Hajkarim, A. Melchiorri, O. Mena, F. Renzi, and Seokhoon Yun, Cosmological bound on the QCD axion mass, redux, J. Cosmol. Astropart. Phys. 09 (2022) 022.
[126] R. L. Workman, V. D. Burkert, V. Crede, E. Klempt, U. Thoma, L. Tiator *et al.*, Review of particle physics, Prog. Theor. Exp. Phys. **2022**, 083C01 (2022).
[127] V. Calvelli, G. Dilasser, W. A. Maksoud, C. Berriaud, F.-P. Juster, J.-p. Lottin *et al.*, 2D and 3D conceptual magnetic design of the MADMAX dipole, IEEE Trans. Appl. Supercond. **30**, 2989478 (2020).
[128] V. Calvelli, F. Nunio, G. Dilasser, W. Abdel Maksoud, C. Berriaud, C. Lorin *et al.*, Advances in the magnetic and mechanical design of the 9 T NbTi MADMAX dipole, IEEE Trans. Appl. Supercond. **33**, 3315201 (2023).
[129] H. Wiedemann, *Particle Accelerator Physics*, 4th ed. (Springer, Cham, 2015), 10.1007/978-3-319-18317-6.
[130] F. Bianchini, G. Grilli di Cortona, and M. Valli, The QCD axion: Some like it hot, arXiv:2310.08169.
[131] HM Treasury and Infrastructure UK, Infrastructure cost review: Technical report, Available at https://www.gov.uk/government/publications/infrastructure-cost-review (2010).
[132] London Bridge Associates Ltd, BTS hyperloop challenge: Tunnels for hyperloop, Available at https://britishtunnelling.com/knowledge/publications/hyperloop (2020).
[133] B. Grose, The hyperloop challenge for tunnelling: Higher productivity and lower costs, Proc. Inst. Civ. Eng. **174**, 71 (2021).
[134] Neat-Aufsichtsdelegation der eidgenössischen Räte, Die Neat-Aufsichtsdelegation der eidgenössischen Räte, Oberaufsicht über den Bau der Neat in den Jahren 2018 und 2019, Technical Report BBl 2020 1397, Sekretariat der parlamentarischen Aufsicht über Finanzen und AlpTransit, Bern, 2020.
[135] P. Fessia, L. Rossi, and S. S. Krog-Pedersen, Application of the learning curve analysis to the LHC main dipole production: First assessment, IEEE Trans. Appl. Supercond. **16**, 242 (2006).
[136] F. Savary, M. Bajko, P. Chevret, G. de Rijk, P. Fessia, P. Lienard *et al.*, Description of the main features of the series production of the LHC main dipole magnets, IEEE Trans. Appl. Supercond. **18**, 220 (2008).
[137] A. Abada, M. Abbrescia, S. S. AbdusSalam, I. Abdyukhanov, J. Abelleira Fernandez, A. Abramov *et al.*, FCC-hh: The hadron collider. Future circular collider conceptual design report volume 3, Eur. Phys. J. Special Topics **228** (2019).
[138] M. Gorghetto and G. Villadoro, Topological susceptibility and QCD axion mass: QED and NNLO corrections, J. High Energy Phys. 03 (2019) 033.
[139] D. J. E. Marsh, Axion cosmology, Phys. Rep. **643**, 1 (2016).
[140] C. A. J. O'Hare, Cosmology of axion dark matter, Proc. Sci. COSMICWISPers (2024) 040 [arXiv:2403.17697].
[141] M. Redi and A. Tesi, Meso-inflationary QCD axion, Phys. Rev. D **107**, 095032 (2023).
[142] K. J. Mack, Axions, inflation and the anthropic principle, J. Cosmol. Astropart. Phys. 07 (2011) 021.
[143] V. B. Klaer and G. D. Moore, How to simulate global cosmic strings with large string tension, J. Cosmol. Astropart. Phys. 10 (2017) 043.
[144] V. B. Klaer and G. D. Moore, The dark-matter axion mass, J. Cosmol. Astropart. Phys. 11 (2017) 049.
[145] A. Vaquero, J. Redondo, and J. Stadler, Early seeds of axion miniclusters, J. Cosmol. Astropart. Phys. 04 (2019) 012.
[146] M. Hindmarsh, J. Lizarraga, A. Lopez-Eiguren, and J. Urrestilla, Scaling density of axion strings, Phys. Rev. Lett. **124**, 021301 (2020).
[147] M. Hindmarsh, J. Lizarraga, A. Lopez-Eiguren, and J. Urrestilla, Approach to scaling in axion string networks, Phys. Rev. D **103**, 103534 (2021).
[148] S. Hoof, J. Jaeckel, and L. J. Thormaehlen, Quantifying uncertainties in the solar axion flux and their impact on determining axion model parameters, J. Cosmol. Astropart. Phys. 09 (2021) 006.
[149] D. M. Lazarus, G. C. Smith, R. Cameron, A. C. Melissinos, G. Ruoso, Y. K. Semertzidis, and F. A. Nezrick, Search for solar axions, Phys. Rev. Lett. **69**, 2333 (1992).
[150] S. Moriyama, M. Minowa, T. Namba, Y. Inoue, Y. Takasu, and A. Yamamoto, Direct search for solar axions by using strong magnetic field and x-ray detectors, Phys. Lett. B **434**, 147 (1998).
[151] Y. Inoue, T. Namba, S. Moriyama, M. Minowa, Y. Takasu, T. Horiuchi, and A. Yamamoto, Search for sub-electronvolt solar axions using coherent conversion of axions into photons in magnetic field and gas helium, Phys. Lett. B **536**, 18 (2002).
[152] Y. Inoue, Y. Akimoto, R. Ohta, T. Mizumoto, A. Yamamoto, and M. Minowa, Search for solar axions with mass around 1 eV using coherent conversion of axions into photons, Phys. Lett. B **668**, 93 (2008).
[153] K. Zioutas, S. Andriamonje, V. Arsov, S. Aune, D. Autiero, F. T. Avignone *et al.*, First results from the CERN axion solar telescope, Phys. Rev. Lett. **94**, 121301 (2005).
[154] S. Andriamonje, S. Aune, D. Autiero, K. Barth, A. Belov, B. Beltrán *et al.*, An improved limit on the axion photon coupling from the CAST experiment, J. Cosmol. Astropart. Phys. 04 (2007) 010.

[155] E. Arik, S. Aune, D. Autiero, K. Barth, A. Belov, B. Beltrán *et al.*, Probing eV-scale axions with CAST, J. Cosmol. Astropart. Phys. 02 (2009) 008.
[156] M. Arik, S. Aune, K. Barth, A. Belov, S. Borghi, H. Bräuninger *et al.*, Search for sub-eV mass solar axions by the CERN axion solar telescope with ^{3}He buffer gas, Phys. Rev. Lett. **107**, 261302 (2011).
[157] K. Barth, A. Belov, B. Beltran, H. Bräuninger, J. M. Carmona, J. I. Collar *et al.*, CAST constraints on the axion-electron coupling, J. Cosmol. Astropart. Phys. 05 (2013) 010.
[158] CAST Collaboration, New CAST limit on the axion-photon interaction, Nat. Phys. **13**, 584 (2017).
[159] E. Armengaud, F. T. Avignone, M. Betz, P. Brax, P. Brun, G. Cantatore *et al.*, Conceptual design of the international axion observatory (IAXO), J. Instrum. **9**, T05002 (2014).
[160] E. Armengaud, D. Attié, S. Basso, P. Brun, N. Bykovskiy, J. M. Carmona *et al.*, Physics potential of the international axion observatory (IAXO), J. Cosmol. Astropart. Phys. 06 (2019) 047.
[161] A. Abeln, K. Altenmüller, S. Arguedas Cuendis, E. Armengaud, D. Attié, S. Aune *et al.*, Conceptual design of BabyIAXO, the intermediate stage towards the international axion observatory, J. High Energy Phys. 05 (2021) 137.
[162] M. E. Gertsenshtein, Wave resonance of light and gravitational waves, J. Exp. Theor. Phys. **14**, 84 (1962).
[163] A. Ejlli, D. Ejlli, A. M. Cruise, G. Pisano, and H. Grote, Upper limits on the amplitude of ultra-high-frequency gravitational waves from graviton to photon conversion, Eur. Phys. J. C **79**, 1032 (2019).
[164] C. Albrecht, S. Barbanotti, H. Hintz, K. Jensch, R. Klos, W. Maschmann *et al.*, Straightening of superconducting HERA dipoles for the any-light-particle-search experiment ALPS II, EPJ Tech. Instrum. **8**, 5 (2021).
[165] N. Phinney, N. Toge, and N. Walker, ILC reference design report volume 3—Accelerator, arXiv:0712.2361.
[166] C. Adolphsen, M. Barone, B. Barish, K. Buesser, P. Burrows, J. Carwardine *et al.*, The international linear collider technical design report—volume 3.I: Accelerator R&D in the technical design phase, arXiv:1306.6353.
[167] P. Bambade, T. Barklow, T. Behnke, M. Berggren, J. Brau, P. Burrows *et al.*, The international linear collider: A global project, arXiv:1903.01629.
[168] S. Hild, S. Chelkowski, and A. Freise, Pushing towards the ET sensitivity using "conventional" technology, arXiv:0810.0604.
[169] M. Punturo, M. Abernathy, F. Acernese, B. Allen, N. Andersson, K. Arun *et al.*, The Einstein Telescope: A third-generation gravitational wave observatory, Classical Quantum Gravity **27**, 194002 (2010).
[170] S. Hild, M. Abernathy, F. Acernese, P. Amaro-Seoane, N. Andersson, K. Arun *et al.*, Sensitivity studies for third-generation gravitational wave observatories, Classical Quantum Gravity **28**, 094013 (2011).
[171] J. A. Fernández Gago and F. Collado Pérez-Seoane, Methodology for the characterisation of linear rail transport infrastructures with the machine learning technique and their application in a hyperloop network, Urban Rail Transit **7**, 159 (2021).
[172] P. Schmuser, Superconducting magnets for particle accelerators, Rep. Prog. Phys. **54**, 683 (1991).
[173] B. Curé, G. Le Godec, M. Ostrega, and U. Wagner, Fifteen years of operation of the compact muon solenoid detector superconducting magnet, IEEE Trans. Appl. Supercond. **34**, 3336838 (2024).
[174] A. Abada, M. Abbrescia, S. S. AbdusSalam, I. Abdyukhanov, J. Abelleira Fernandez, A. Abramov *et al.*, FCC-ee: The lepton collider. Future circular collider conceptual design report volume 2, Eur. Phys. J. Spec. Top. **228**, 261 (2019).
[175] H. Lierl and S. Wolff, Superconducting magnet and cryogenic system of HERA, J. Cryog. Supercond. Soc. Jpn. **31**, 360 (1996).
[176] O. S. Brüning, P. Collier, P. Lebrun, S. Myers, R. Ostojic, J. Poole *et al.*, LHC design report, Technical Report No. CERN-2004-003-V-1, CERN, Geneva, 2004, 10.5170/CERN-2004-003-V-1.
[177] H. T. Edwards, The tevatron energy doubler: A superconducting accelerator, Annu. Rev. Nucl. Part. Sci. **35**, 605 (1985).
[178] European GNSS Agency, Galileo high accuracy service (HAS). Info note, Technical Report No. TS-02-20-910-EN-N, European GNSS Agency, Prague, 2020, 10.2878/581340.
[179] A. Zeiner, GNSS monitoring for safety on the Brenner, Reporter **68**, 26 (2013).
[180] BBT SE, The Brenner Base Tunnel—A new link below the Alps, Published online at https://www.bbt-se.com/fileadmin/broschueren/2022/general-brochure-en (2022).
[181] G. Arduini (private communication).
[182] K. Perlin, Noise, hypertexture, antialiasing, and gesture, in *Texturing and Modeling (Third Edition)*, The Morgan Kaufmann Series in Computer Graphics (Morgan Kaufmann, San Francisco, 2003), pp. 336–410, 10.1016/B978-155860848-1/50041-3.
[183] E. Todesco, B. Bellesia, P. Hagen, and C. Vollinger, Trends in field quality along the production of the LHC dipoles and differences among manufacturers, IEEE Trans. Appl. Supercond. **16**, 419 (2006).
[184] J. Galan, J. von Oy, K. Jakovcic, F. Rodríguez Candón, J. A. García, L. A. Obis Aparicio *et al.*, Rest-for-physics/axionlib: v2.2, Zenodo, 10.5281/zenodo.10650613 (2024).
[185] H. A. Enge, Effect of extended fringing fields on ion-focusing properties of deflecting magnets, Rev. Sci. Instrum. **35**, 278 (1964).
[186] A. Wolski, *Beam Dynamics in High Energy Particle Accelerators* (Imperial College Press, London, UK, 2014), 10.1142/p899.